



저작자표시-비영리-변경금지 2.0 대한민국

이용자는 아래의 조건을 따르는 경우에 한하여 자유롭게

- 이 저작물을 복제, 배포, 전송, 전시, 공연 및 방송할 수 있습니다.

다음과 같은 조건을 따라야 합니다:



저작자표시. 귀하는 원저작자를 표시하여야 합니다.



비영리. 귀하는 이 저작물을 영리 목적으로 이용할 수 없습니다.



변경금지. 귀하는 이 저작물을 개작, 변형 또는 가공할 수 없습니다.

- 귀하는, 이 저작물의 재이용이나 배포의 경우, 이 저작물에 적용된 이용허락조건을 명확하게 나타내어야 합니다.
- 저작권자로부터 별도의 허가를 받으면 이러한 조건들은 적용되지 않습니다.

저작권법에 따른 이용자의 권리는 위의 내용에 의하여 영향을 받지 않습니다.

이것은 [이용허락규약\(Legal Code\)](#)을 이해하기 쉽게 요약한 것입니다.

[Disclaimer](#)

공학박사 학위논문

**Development of Au or Pt supported  
TiO<sub>2</sub> photocatalytic materials in the  
morphological, crystal phase, and  
band bending aspects**

형태, 결정상, 밴드 굽힘을 고려한 금 또는  
백금이 담지된 이산화티탄 광촉매 물질의 개발

2020년 2월

서울대학교 대학원

화학생물공학부

송 찬 경

## Abstract

# **Development of Au or Pt supported TiO<sub>2</sub> photocatalytic materials in the morphological, crystal phase, and band bending aspects**

Chyan Kyung Song

School of Chemical and Biological Engineering

The Graduate School

Seoul National University

In order to solve the environmental pollution occurring around the world, it is essential to develop a catalytic system based on readily available energy sources. Photocatalytic systems have received a lot of attention, since those do not require additional waste of energy for the use of catalysts and can be used wherever light is present. In this study, noble metal supported titanium dioxide (TiO<sub>2</sub>) systems were synthesized based on the concept that noble metal nanoparticles like Au and Pt can utilize visible light in photocatalysis. TiO<sub>2</sub> is a generally used semiconductor material due to chemical stability, nontoxicity and economically availability, although having the inferior property of hardly absorbing light in the visible light region. However, TiO<sub>2</sub> is a strong candidate as photocatalytic material by supporting metal nanoparticles which assists to utilize visible light. Methodologies were suggested for enhancing photocatalytic performance focusing on the metal-TiO<sub>2</sub> systems.

The phase and morphology of TiO<sub>2</sub> were optimized to enhance a

photocatalytic performance under visible light region. It was identified that rutile phase  $\text{TiO}_2$  of three dimensional structure is the most probable photocatalytic system among Au/ $\text{TiO}_2$ . Local surface plasmonic resonance (LSPR) life time of gold nanoparticles prolonged and efficient plasmonic interaction occurred due to the three dimensional morphology of  $\text{TiO}_2$ , and photocatalytic performance was observed to be increased. Furthermore, hot electrons generated from LSPR more efficiently transfer to rutile  $\text{TiO}_2$  than anatase  $\text{TiO}_2$ . Hot electrons can favorably transfer from Au to rutile  $\text{TiO}_2$  due to the overlapping DOS of Au and rutile  $\text{TiO}_2$  conduction band, and the electron transfer of opposite direction could be blocked by larger band bending of rutile  $\text{TiO}_2$ .

Energetic alignments of metal-semiconductor systems were modulated to improve a charge separation between interfaces. Lowering of Fermi level can be obtained by reducing a size of metal nanoparticle to a few nanometer scale, and those change altered an extent of band bending in a semiconductor material. Pt-rutile  $\text{TiO}_2$  material was selected as a model system, and Pt nanoparticles were positively charged under visible light irradiation. The rate and amount of charge separation were more improved when the extent of band bending was increased in the  $\text{TiO}_2$  interface. When charge separation rates between Pt- $\text{TiO}_2$  interfaces and activities for photocatalytic oxidation were comparatively analyzed, those results are deeply related. The efficient charge separation is decided to be the major factor for the enhanced photocatalytic performance.

**Keywords:** Heterogeneous catalyst, Photocatalyst, Charge separation, energy level, local surface plasmon resonance, Titanium dioxide, gold, platinum

**Student Number:** 2014-21589

# Contents

Contents iii

<b>Chapter 1. Introduction.....</b>	<b>1</b>
1.1 Photocatalysis under visible light using metal nanoparticle supported TiO <sub>2</sub> materials .....	1
1.2 Exploring crystal phase and morphology of the TiO <sub>2</sub> supporting materials.....	3
1.3 Modulation of band bending extent between a metal-support interface .....	5
1.4. Objectives .....	6
<b>Chapter 2. Crystal Phase and Morphology of the TiO<sub>2</sub> Supporting Materials Used for Visible-Light Driven Plasmonic Photocatalyst.....</b>	<b>7</b>
2.1 Introduction.....	7
2.2 Experimental .....	10
2.2.1 Preparation of Au/TiO <sub>2</sub> heterostructures .....	10
2.2.2 Photocatalytic activity test.....	12
2.2.3 Characterization of materials.....	12
2.2.4 Photoluminescence test .....	13
2.2.5 Computational details .....	14
2.3 Results and discussion .....	16
2.3.1 Physicochemical and optical property of 2 wt.% Au/TiO <sub>2</sub> .....	16
2.3.2 Photocatalytic degradation of RNO.....	17
2.3.3 Effect of morphology in rutile phase TiO <sub>2</sub> .....	19
2.3.4 Interfacial charge transfer rate comparison in 2 wt.% Au/TiO <sub>2</sub> heterostructures.....	20

2.3.5 Discussion of different energy band diagram between Au/anatase TiO <sub>2</sub> and Au/rutile TiO <sub>2</sub> .....	22
<b>Chapter 3. Modulating energetic alignment of Pt-TiO<sub>2</sub> system for enhanced charge separation directly related to a photocatalytic performance.....</b>	<b>50</b>
<b>3.1 Introduction.....</b>	<b>50</b>
<b>3.2 Experimental .....</b>	<b>53</b>
3.2.1 Synthesis of Pt/TiO <sub>2</sub> photocatalysts with various Pt sizes.....	53
3.2.2 Characterization.....	54
3.2.3 Electrochemical characterization .....	55
3.2.4 Photoluminescence spectroscopy .....	56
3.2.5 Calculation of the interfacial area between Pt and TiO <sub>2</sub> .....	57
3.2.6 Calculation of the external monolayer volume to total volume ratio of Pt NPs.....	59
3.2.7 Finding the relationship between hole transfer and electron transfer between the Pt-TiO <sub>2</sub> interface under light irradiation conditions .....	60
<b>3.3 Results and discussion .....</b>	<b>63</b>
3.3.1 Physicochemical properties of Pt/TiO <sub>2</sub> s .....	63
3.3.2 Band alignment modulations of Pt/TiO <sub>2</sub> systems .....	66
3.3.3 Observations of charge separation between Pt-TiO <sub>2</sub> interfaces under visible light.....	68
3.3.4 Kinetic analysis of charge separation between Pt-TiO <sub>2</sub> interfaces .....	69
3.3.5 Photocatalytic activity test.....	71
<b>Chapter 4. Summary and Conclusions .....</b>	<b>92</b>
<b>Bibliography .....</b>	<b>94</b>
<b>국 문 초 록 .....</b>	<b>102</b>

# List of Tables

Table 2-1. The final content of Au in a series of Au/TiO <sub>2</sub> s calculated from ICP-AES.....	24
Table 2-2. BET surface area, pore volume, and average pore diameter of the synthesized 2 wt.% Au/TiO <sub>2</sub> heterostructures .....	25
Table 2-3. Kinetic parameters extracted from fitted results of time-resolved PL spectra .....	26
Table 2-4. Electron transfer paths, governing equations, and analytical solutions in a RhB solution, TiO <sub>2</sub> in a RhB solution, and Au/TiO <sub>2</sub> in a RhB solution with an excitation wavelength of 500 nm.....	27
Table 2-5. Electron transfer rate constants of Au/TiO <sub>2</sub> in the presence of RhB. The kinetic parameters were extracted from the fitted results of time-resolved PL spectra (Table 2-3), and electron transfer rate constants were calculated by electron transfer paths described in Table 2-4.....	28
Table 2-6. DFT calculation results for Au/anatase and Au/rutile. Binding energies of every possible sites, the most stable structure, and DOS spectra coming from those structures are listed. In the DOS spectra, dashed lines indicate CB minimum and VB maximum of TiO <sub>2</sub> , and continuous lines indicate E <sub>F</sub> of Au/TiO <sub>2</sub> . E <sub>F</sub> of TiO <sub>2</sub> matches with VB maximum line.....	29
Table 3-1. Measurement of the Pt element concentration in Pt(x)/TiO <sub>2</sub> systems according to ICP analysis. ....	73
Table 3-2. Calculated external surface area of Pt(x) and the interfacial area of Pt(x)/TiO <sub>2</sub> . Experimentally measured surface area of Pt(x)/TiO <sub>2</sub> and Pt(x) based on BET and CO adsorption analysis. ....	74
Table 3-3. Kinetic parameters extracted from fitted results of the time-resolved	

PL spectra. The first PL is from Rhodamine B, and the second is from TiO <sub>2</sub> .....	75
Table 3-4. Calculating processes of governing equations for charge transfer rate constants, and electron transfer rate constants in RhB, TiO <sub>2</sub> in RhB, and Pt(x)/TiO <sub>2</sub> in RhB. The hole-transfer rate constants were particularly important to consider in the Pt(x)/TiO <sub>2</sub> s. ....	76
Table 3-5. Charge-transfer rate constants of TiO <sub>2</sub> and Pt(x)/TiO <sub>2</sub> systems derived from the fitted results of the time-resolved PL spectra, according to processes used for calculation (Table 3-4).....	77

# List of Figures

Figure 2-1. Schematic diagram for the preparing methods of a series of TiO <sub>2</sub> s.....	30
Figure 2-2. FE-SEM image, N <sub>2</sub> adsorption-desorption isotherm, and pore size distribution for (a) Au/SAna, (b) Au/LAna, (c) Au/RAna, (d) Au/P 25, (e) Au/RRut, and (f) Au/3DRut.....	31
Figure 2-3. EDS spectra of a series of Au/TiO <sub>2</sub> s. (a) Au/SAna, (b) Au/LAna, (c) Au/RAna, (d) Au/RRut, and (e) Au/3DRut.....	32
Figure 2-4. X-ray photoemission spectra of a series of Au/TiO <sub>2</sub> s. In the ranges of Au 4f and Ti 2p were observed..	33
Figure 2-5. HR-TEM images of a series of 2 wt.% Au/TiO <sub>2</sub> heterostructures. Au/3DRut-1: High-magnified image and Au/3DRut-2: low magnified image, (SAna: small anatase TiO <sub>2</sub> spheres, BAna: large anatase TiO <sub>2</sub> spheres, RAna: anatase TiO <sub>2</sub> rods, RRut: rutile TiO <sub>2</sub> rods, and 3DRut: 3D hierarchical rutile TiO <sub>2</sub> )..	34
Figure 2-6. Au size distribution for (a) Au/SAna, (b) Au/LAna, (c) Au/RAna, (d) Au/P 25, (e) Au/RRut, and (f) Au/3DRut.....	35
Figure 2-7. HADDF-STEM images of 2 wt.% Au/3DRut. 2D atom mappings of Ti, O, and Au were conducted and are noted.....	36
Figure 2-8. XRD spectra with calculated TiO <sub>2</sub> crystallite sizes of a series of 2 wt.% Au/TiO <sub>2</sub> heterostructures. In the absorption part of LSPR, units of axis were converged for calculations of LSPR linewidth and indicated inset.....	37
Figure 2-9.(a) HR-TEM images of Au/3DRut. The image was firstly obtained in 200 nm scale and magnified to 20 nm scale for the identification of rutile crystallite. (b) FFT patterns obtained from the magnified HR-TEM image.....	38
Figure 2-10. UV-Vis DRS spectra of a series of 2 wt.% Au/TiO <sub>2</sub>	

heterostructures. In the absorption part of LSPR, units of axis were converged for calculations of LSPR linewidth and indicated inset .....	39
Figure 2-11. UV-Vis DRS spectra of a series of TiO <sub>2</sub> s. ....	40
Figure 2-12. Photocatalytic degradation of RNO in the presence of a series of 2 wt.% Au/TiO <sub>2</sub> heterostructures under visible light (>455 nm filter).....	41
Figure 2-13. Hydroxyl radical formation path in Au/TiO <sub>2</sub> under visible light. RNO is degraded by hydroxyl radical. ....	42
Figure 2-14. FT-IR spectra of a series of Au/TiO <sub>2</sub> s. FT-IR spectra in the range of 3600-3100 cm <sup>-1</sup> represents surface hydroxyl group.....	43
Figure 2-15. (a), (b) Below are dark field images of Au/3DRut and Au/RRut. Typical particles were selected and are indicated by red circles. Dark-field scattering spectra were obtained from corresponding particles and normalized with BET surface area.....	44
Figure 2-16. (a) FDTD simulations were performed according to inset scheme of coupled Au NPs with light irradiation in different directions. Derived wavelength and intensity were presented, and the values of original 10 nm Au NP were indicated by dotted lines. (b) TEM images of Au/3DRut and Au/RRut are listed above. Simplified schemes of Au/3DRut and Au/RRut including light irradiation are contained below.....	45
Figure 2-17. (a) TR-PL spectra of Au/TiO <sub>2</sub> in RhB solution. (b) $k_{R \rightarrow A \rightarrow T}$ values of a series of Au/TiO <sub>2</sub> heterostructures. The values were derived from parameters obtained from TR-PL spectra.....	46
Figure 2-18. Time-resolved PL spectra of TiO <sub>2</sub> in the presence of 1 μM RhB solution. All fitting parameters are described and summarized in Table 2-3. ....	47

Figure 2-19.(a), (b) Steady-state PL (SSPL) spectra of a 1 $\mu$ M RhB solution measured in the emission mode at an excitation wavelength of 500 nm and the excitation mode at an emission wavelength of 580 nm. (c) SSPL spectra of a series of TiO <sub>2</sub> heterostructures and Au/TiO <sub>2</sub> in D.I. water measured with excitation mode at 580 nm emission wavelength. 2.5 nm slit was used for the measurements. (d) SSPL spectra of a series of Au/TiO <sub>2</sub> heterostructures in D.I. water. To magnify emission spectra at 580 nm, 10 nm slit was used for the measurement.....	48
Figure 2-20. Schematic energy band diagram of two types of Au/TiO <sub>2</sub> , showing the proposed electron transfer processes under visible light. ....	49
Figure 3-1. TEM and Cs-TEM images of Pt(1.7)/TiO <sub>2</sub> , Pt(3.3)/TiO <sub>2</sub> , and Pt(5.1)/TiO <sub>2</sub> . Each x value in Pt(x)/TiO <sub>2</sub> systems means an averaged Pt nanoparticle size. Scale bars in Cs-TEM images indicate 1 nm. FFT patterns were obtained from a Pt NP in the Cs-TEM images. ....	78
Figure 3-2. Pt NP size distributions in (a) Pt(1.7)/TiO <sub>2</sub> , (b) Pt(3.3)/TiO <sub>2</sub> , and (c) Pt(5.1)/TiO <sub>2</sub> .....	79
Figure 3-3. UV-Vis DRS spectra of Pt(x)/TiO <sub>2</sub> systems. ....	80
Figure 3-4. X-ray diffraction spectra of Pt(x)/TiO <sub>2</sub> systems.....	81
Figure 3-5. (a) Ti 2p and (b) O 1s XPS spectra of Pt(1.7)/TiO <sub>2</sub> , Pt(3.3)/TiO <sub>2</sub> , Pt(5.1)/TiO <sub>2</sub> and TiO <sub>2</sub> .....	82
Figure 3-6. Pt 4f XPS spectra of Pt(1.7)/TiO <sub>2</sub> , Pt(3.3)/TiO <sub>2</sub> , Pt(5.1)/TiO <sub>2</sub> and TiO <sub>2</sub> . ....	83
Figure 3-7. Pt L3 edge XANES spectra of Pt(x)/ TiO <sub>2</sub> s before and after visible light irradiation condition. The enlarged ranges show the white line differences. ....	84
Figure 3-8. (a) Mott–Schottky plot of TiO <sub>2</sub> and Pt(x)/TiO <sub>2</sub> systems for the observation of flat band potential under dark condition. (b)	

	Schematic energy diagrams of Pt/TiO <sub>2</sub> systems with Pt NP size variation when visible light is irradiated. ....	85
Figure 3-9.	(a) Time-resolved photoluminescence spectra (PL) of TiO <sub>2</sub> and Pt(x)/TiO <sub>2</sub> systems in the RhB solutions with 580 nm emission where laser excitation was 405 nm. (b) Charge transfer path of Pt/TiO <sub>2</sub> in the time-resolved PL measurement condition. Electron transfer rate constants were denoted as black and blue arrows, and a hole transfer rate as red arrows. ....	86
Figure 3-10.	Electron transfer paths under conditions of (a) a RhB solution, (b) TiO <sub>2</sub> in the RhB solution, and (c) Pt(x)/TiO <sub>2</sub> in the RhB solution with a laser excitation wavelength of 405 nm and an emission wavelength of 580 nm. ....	87
Figure 3-11.	Two congruent pictures at the point of kinetics. When a product of electron and hole carrier concentration remains constant, (a) the hole transfer from the TiO <sub>2</sub> VB to Pt ( $k_{T \rightarrow P}^+$ ) can be treated as (b) an electron transfer from Pt to the TiO <sub>2</sub> CB ( $-k_{T \rightarrow P}^+$ ) according to the mathematical consequence. ....	88
Figure 3-12.	Comparison of acetaldehyde conversion rates and charge separation rate constants. The acetaldehyde oxidation rate, which is related to hole consumption, was indicated by gray bar. The hole transfer rate ( $k_{T \rightarrow P}^+$ ) was expressed by red line and the electron transfer rate ( $k_{R \rightarrow P \rightarrow T}$ ) by blue line. ....	89
Figure 3-13.	Photocatalytic rate of Pt(x)/TiO <sub>2</sub> in acetaldehyde oxidation under (a) visible light irradiation (>400 nm) and (b) dark conditions with an enlarged inset. ....	90
Figure 3-14.	Schematic mechanism for acetaldehyde photodegradation by hole consumption, which could be generated by the hole transport from TiO <sub>2</sub> and the hot electron generation from Pt. ....	91

# **Chapter 1. Introduction**

## **1.1 Photocatalysis under visible light using metal nanoparticle supported TiO<sub>2</sub> materials**

Catalyst enables impregnable chemical reactions using various energy sources including heat, light, and electricity. Photocatalysis is getting a lot of attention due to the extensive applicability anywhere light exists and the economic feasibility without additional energy consumption. Photocatalytic redox reactions can occur by separating electrons and holes in semiconductor, and available light range is varied depending on the size of the bandgap. Although small band gap materials can absorb and use broad ranges of light including long wavelength, those materials are degraded under light irradiation. Semiconductor materials absorbing light of shorter wavelength than ultraviolet ray are generally stable. Only 3% of light is consisted of ultraviolet ray reaching the earth, and developing stable photocatalytic materials absorbing visible light is an important matter. As part of its efforts, recent studies have been reported that several kinds of metal nanoparticles can absorb visible light by local surface plasmon resonance (LSPR) and generate hot electrons can be directly used in the photocatalysis [1-8]. Thus, when metal nanoparticles supported on

middle bandgap semiconductor materials, those systems could be strong candidates for stable and visible light active photocatalysts. In this study, noble metal supported TiO<sub>2</sub> materials are studied to understand fundamental aspects and develop an advanced photocatalytic system effectively operates in sunlight.

## **1.2 Exploring crystal phase and morphology of the TiO<sub>2</sub> supporting materials**

In recent researches directed at photocatalysis, plasmonic noble metal supported on a semiconductor is one of the promising topics, since this material can be activated under visible light [9-16]. The main focuses in this area have been on applying various semiconductor materials [17,18], regulating morphologies [19,20], and designing efficient multi-heterojunction materials [21-23]. For the rationally and entirely considered design of plasmonic photocatalyst material, microscopic aspect of metal-semiconductor interface and optical aspect coming from morphology need to be considered at the same time.

TiO<sub>2</sub> is one of the most widely investigated semiconductor material in photocatalysis because of low cost, non-toxic and high chemical stability [24]. It is still a controversial issue that which phase of TiO<sub>2</sub> is appropriate for plasmonic photocatalysis. It is generally known that, anatase TiO<sub>2</sub> is more effective than rutile TiO<sub>2</sub> in conventional photocatalysis in the UV light region by virtue of the facile electron-hole separation and higher exciton mobility [25-27]. There are a few reports indicating that the photocatalytic activity of gold-loaded rutile TiO<sub>2</sub> (Au/rutile TiO<sub>2</sub>) is better than Au/anatase TiO<sub>2</sub> under

conditions of visible light irradiation. It was reported that elongation of the LSPR lifetime in the Au/rutile system favors the interfacial electron transfer from Au to rutile TiO<sub>2</sub> [28,29], but there is no quantitative evidence for why Au/rutile TiO<sub>2</sub> is superior than Au/anatase TiO<sub>2</sub>. Importantly, these reports support our argument that those criteria should be reconsidered in the aspect of microscopic and optical for plasmonic photocatalysis.

### **1.3 Modulation of band bending extent between a metal-support interface**

Electron-hole separation occurring at the metal-semiconductor (M-S) interface is a key concept in enhancing the performance of M-S photocatalytic systems [30-33]. The charged state of metal parts should be elastically modulated in either a positive or negative direction in accordance with target oxidation or reduction reactions when light irradiates M-S interfaces. In most general M-S photocatalytic systems where semiconductor materials are operated as electron-hole formation sources, a negative charged state of metal is commonly introduced and applied to target reduction reactions, and studies have sought to explain the electron transfer path and its mechanisms [34-36]. Likewise, positive charge should be induced to metal cocatalyst for photocatalytic oxidation reactions, although there is a lack of discussion about charge separation methodology and charge carrier transfer paths [37,38]. Therefore, for the development of a M-S system that utilizes metal in a positively charged state, a Pt/rutile TiO<sub>2</sub> system was selected as a representative M-S catalyst. The Pt/TiO<sub>2</sub> system was devised to be controllable for charge separation extent between the M-S interface, and applied to the degradation of a gaseous volatile organic material to determine how a positive charge accumulation on metal affects the photocatalytic oxidation reaction rates.

## 1.4. Objectives

The objectives of this thesis are developing noble metal supported  $\text{TiO}_2$  materials for photocatalysts operating under visible light, and enhancing photocatalytic activity for environmental applications by optimizing  $\text{TiO}_2$  material and metal- $\text{TiO}_2$  energetic alignment.

In following section, Chapter 2 reports the optimization of  $\text{TiO}_2$  supporting materials in phase and morphological aspects. There is a controversy about which phase of  $\text{TiO}_2$  is appropriate for photocatalyst under visible light. In this work, the argument was considered by combining experimental analysis and theoretical calculation. The morphology was rationally controlled to increase a photocatalytic performance.

Chapter 3 discusses modulations of band bending extent between metal- $\text{TiO}_2$  interfaces focusing on energetic alignment of materials. Band bending at the interface affect charge separation, which are the main factors for photocatalytic operation. Charge separation amount and rate are observed and analysed under visible light irradiation.

# **Chapter 2. Crystal Phase and Morphology of the TiO<sub>2</sub> Supporting Materials Used for Visible-Light Driven Plasmonic Photocatalyst**

## **2.1 Introduction**

In the microscopic aspect of metal-semiconductor interface, semiconductor material with high electric permittivity can contribute to large amount of charge separation between metal and semiconductor, when proper metal-semiconductor bonding and Fermi energy ( $E_F$ ) level difference exist. TiO<sub>2</sub> is one of the strong candidates among semiconductor materials, especially rutile TiO<sub>2</sub> polymorphs, exhibits relatively large permittivity ( $\epsilon(\text{rutile TiO}_2) = 114$  and  $\epsilon(\text{anatase TiO}_2) = 48$ ).  $E_F$  and band level of TiO<sub>2</sub> are well suited with  $E_F$  of plasmonic noble metal for the formation of Schottky barrier, which acts as obstacle for electron transfer from TiO<sub>2</sub> to Au but enables electron transfer from Au to TiO<sub>2</sub> by local surface plasmon resonance (LSPR).

Furthermore, in the optical aspect, 3D morphology of semiconductor as a supporting material decorated with plasmonic metal nanoparticles can modulate the direction of light irradiation on the coupled nanoparticles. In the closely spaced Au nanoparticle arrays, it is observed that transverse or longitudinal mode of plasmonic interaction happens, respectively depending on irradiated light direction, which affects the LSPR wavelength and extinction intensity [39].

In the light of this feature, it is expected that radially symmetric 3D mesoporous structure material can get irradiated light with the same direction regardless of orientation, although randomly oriented 0D sphere, 1D rod, or 2D sheet structure material cannot have any priority in direction of light irradiation.

In the present study, complementary approaches of experimental and computational analyses are attempted to explore and disclose that how the crystal phase and morphology of TiO<sub>2</sub> influence plasmonic photocatalytic activity. The TiO<sub>2</sub> samples used in this work were small anatase TiO<sub>2</sub> spheres (SA), large anatase TiO<sub>2</sub> spheres (LA), anatase TiO<sub>2</sub> rods (RA), rutile TiO<sub>2</sub> rods (RR), and 3D hierarchical rutile TiO<sub>2</sub> (3DR). Based on these materials, 2 wt.% Au/TiO<sub>2</sub> heterostructures were synthesized by a deposition-precipitation method. *p*-nitrosodimethylaniline (RNO) was representatively used for the measurement of plasmonic photocatalytic activity of a series of Au/TiO<sub>2</sub>s. RNO is a dye which can only be degraded by hydroxyl radical [40], which indicates that self photodegradation or photodegradation by direct charge transfer between Au/TiO<sub>2</sub> and adsorbed RNO is negligible. Hydroxyl radical has been known to be the main component for the degradation of organic compounds. Dark field microscope (DFM) and a finite-difference time-domain (FDTD) simulation was conducted to identify the morphological aspect, and time-resolved photoluminescence (TR-PL) and density functional theory (DFT) calculations to the microscopic aspect.

Results presented here highlight LSPR lifetime of hot electrons, plasmonic interaction effect in the morphological aspect, interfacial electron transfer rate between Au and TiO<sub>2</sub>, Au density of states (DOS), and band bending in the

crystal phase aspect, respectively. Our results provide insight into the factors important to design heterostructure using  $\text{TiO}_2$  as supporting material for photocatalyst under visible light ( $>455$  nm).

## 2.2 Experimental

### 2.2.1 Preparation of Au/TiO<sub>2</sub> heterostructures

TiO<sub>2</sub>s were synthesized to have different morphology and phase. Figure 2-1 shows the schematic diagram for the fabrication process of a series of TiO<sub>2</sub>s. Three types of anatase TiO<sub>2</sub> particles were prepared, as described in our previous report [41]. Small anatase TiO<sub>2</sub> spheres (SAna) were synthesized by the gel-sol method. A 0.4 mol triethanolamine ( $\geq 98\%$ , Aldrich) and a 0.2 mol titanium(IV) isopropoxide ( $\geq 99.0\%$ , Samchun) were mixed for 30 min, and deionized water (D.I. water) was then added to a total volume of 400 ml, followed by mixing for 30 min until the color of the solution changed to yellow. A 30 ml aliquot of this solution was added to 30 ml of 0.02 M oleic acid (Samchun), which was used as a surfactant. The mixtures were transferred to a Teflon-lined autoclave and heated at 100 °C for 12 h and then at 250 °C for 48 h. The light red colored precipitate obtained was washed three times with D.I. water and isolated by centrifugation. The product was dried at 70 °C for 12 h and calcined at 450 °C for 8 h. LAna and RAna were synthesized by varying the type of surfactant and hydrothermal treatment time. Diethylamine was used as a surfactant in LAna and diethylenetriamine in RAna. The hydrothermal treatment process was 100 °C for 24 h and then 250 °C for 72 h both in case of large anatase TiO<sub>2</sub> spheres (LAna) and anatase TiO<sub>2</sub> rods (RAna). 3D hierarchical rutile TiO<sub>2</sub> (3DRut) was synthesized by a micro-emulsion method [42]. Briefly, titanium n-butoxide (TiBu, 97%, Aldrich) was used as the TiO<sub>2</sub>

precursor and magnesium stearate (Riedel-de Haën) was used as the surfactant. Aqueous and oil crystal phases were separately prepared and then mixed. In the case of the aqueous crystal phase, 30 ml of 2.6 M hydrochloric acid (35~37%, Samchun) was mixed with 0.7686 g magnesium stearate. In the case of the oil crystal phase, 4.5 ml n-amyl alcohol (99 %, Samchun) was added to 30 ml of cyclohexane ( $\geq 99\%$ , Aldrich) as a cosolvent and 4.0 ml TiBu was mixed with that solution. The oil phase was first stirred for 20 min before mixing and then stirred for 30 min after mixing. The total solution was transferred to a Teflon-lined autoclave and subjected to a heat treatment at 150 °C for 4 h. The resulting precipitate was centrifuged with D.I. water and ethanol (1:1, v/v) for several times, dried at 70 °C for 12 h and then calcined at 550 °C for 4 h. Rutile TiO<sub>2</sub> rods (RRut) was produced from 3DRut by ultrasonication treatment for 36 h at the concentration of 1 g TiO<sub>2</sub>/30 ml D.I. water. The final product was then collected by centrifugation and dried at 70 °C for 12 h.

All Au/TiO<sub>2</sub> heterostructures are prepared with 2 wt.% of Au loading. The 2 wt.% Au/TiO<sub>2</sub> heterostructures were synthesized by deposition-precipitation method. A 0.3 g sample of the prepared TiO<sub>2</sub> sample was added to a 100 ml of HAuCl<sub>4</sub>·4H<sub>2</sub>O ( $\geq 99.9\%$ , Aldrich) solution, which contained the same equivalent of 0.006 g of Au. The pH was then adjusted to  $\sim 7$  with a 0.05 M NaOH ( $\geq 98.0\%$ , Samchun) solution prior to stirring for 12 h in dark condition. Since then, 50 ml of NaBH<sub>4</sub> (99%, Aldrich) solution containing NaBH<sub>4</sub> 10 times more than of the amount of Au was dropwisely injected to the solution and stirred for 1 h. The product was centrifuged and washed with D.I. water for several times, and finally dried at 70 °C for 12 h.

### **2.2.2 Photocatalytic activity test**

RNO was selected as a representative organic compound for photodegradation because RNO is only degraded by hydroxyl radicals. Hydroxyl radicals are known to be the main component in the degradation of organic matter. 0.1 g of Au/TiO<sub>2</sub> photocatalyst was added to 100 ml of 3 ppm RNO solution and dispersed by stirring for 5 h in the dark. The photodegradation was then conducted under visible light, using a 300 W Xe lamp with a 455 nm cut-on filter. The decrease in the concentration of RNO was measured by UV-Vis spectroscopy (V670-Jasco) in the range of 200-800 nm at an interval of 1 h after filtering the catalyst. Absorbance at 439 nm wavelength was identified as the highest and used for the analysis of first-order reaction based photodegradation rate constants.

### **2.2.3 Characterization of materials**

The shapes of the TiO<sub>2</sub> and gold nanoparticle size distribution were observed by high-resolution transmission electron microscopy (HR-TEM, JEM 3010- JEOL, 300 kV) equipped with energy-dispersive X-ray spectroscopy (EDS, Oxford) and field-emission scanning electron microscopy (FE-SEM, SUPRA 55VP, Carl Zeiss). The elemental chemical status was observed by X-ray photoelectron spectroscopy (XPS, AXIS-HSi, KRATOS). The final content of Au in a series of Au/TiO<sub>2</sub>s was determined by inductive coupled plasma atomic emission spectrometry (ICP-AES, OPTIMA 4300DV). The crystal phases of

Au/TiO<sub>2</sub> were defined by X-ray diffractometry (XRD, D/max-2500/PC-Rigaku) with Cu K $\alpha$  radiation ( $\lambda = 1.5406 \text{ \AA}$ ) as an incident beam at operating mode of 50 kV and 100 mA. N<sub>2</sub> adsorption-desorption analysis was conducted at 77 K using ASAP 2010 (Micromeritics). The surface area of Au/TiO<sub>2</sub> was calculated by the BET method in the range of  $P/P_0 = 0.1-0.2$ . Pore size distribution and pore volume were obtained from the absorption branches using BJH methods. Analytical high-angle annular dark-field scanning transmission electron microscope (HAADF-STEM, Tecnai F20-FEI, 200 kV) equipped with EDS (Tecnai 136-5-EDAX) was used for 2D atomic mapping of Ti, Au, and O. FT-IR spectrophotometer (Nicolet 6700) was used to identify the amount of surface hydroxyl group in a series of Au/TiO<sub>2</sub>s. The dark-field micro-spectroscopic system is a combination of a commercial Axio Observer Z1 inverted microscope (Carl Zeiss, Germany), a true-color digital camera, a 1024 pixel 256 pixel cooled spectrograph CCD camera (Andor Technology PLC, UK) and a home-built micro-fluidic chamber. The spectrophotometer (Monora320i, Dongwoo Optron Co., Korea) had dual-turret holding gratings of 1200 grooves/mm and 300 grooves/mm. A programmable shutter was mounted internal to an adjustable entrance slit, the width of which could be opened to retain only a single nanoparticle in the region of interest.

#### **2.2.4 Photoluminescence test**

All photoluminescence (PL) data were obtained at a concentration of 0.01 g of sample/10 ml of solution, which is the same conditions as were used in the

photodegradation test. PerkinElmer LS55 spectrophotometer (PerkinElmer Ltd., Beaconsfield, UK) equipped with a Xe lamp was used for the measurement of steady-state PL of a series of TiO<sub>2</sub> and Au/TiO<sub>2</sub> heterostructures. Time-resolved PL was measured by using 1  $\mu$ M of rhodamine B dye (RhB, Aldrich, for fluorescence) solution according to time correlated single photon counting methods by using FluoTime 200 instrument (Picoquant GmbH). A 500 nm pulsed diode laser (LDH-P-C-500, Picoquant GmbH, pulse energy = 10 pJ; FWHM < 54 ps) with the repetition rate of 80 MHz was used as an excitation source. The measured results from the PicoHarp 300 were analyzed by the FluoFit software.

### **2.2.5 Computational details**

OptiFDTD version 12.0 was used to perform the FDTD simulations. Two 10 nm size Au NPs were located inside a 0.6  $\mu$ m  $\times$  0.3  $\mu$ m  $\times$  0.3  $\mu$ m domain. In the case of two coupled Au NPs, the gap was designated to 2 nm, whereas 100 nm for two independent Au NPs. Mesh parameters were 0.001  $\mu$ m  $\times$  0.001  $\mu$ m  $\times$  0.001  $\mu$ m, and time step size was 1.668e<sup>-018</sup> with 12000 time steps. A 550 nm wavelength rectangular Gaussian modulated continuous wave was directed along the z-axis, and a discrete Fourier transform between 0.4  $\mu$ m  $\sim$  0.9  $\mu$ m was performed to derive power spectrum of Au NPs. Periodic boundary condition (PBC) was applied to x and y-direction, and anisotropic perfectly matched layer (APML) to z-direction to perform the FDTD simulation.

Periodic density functional theory (DFT) calculations were carried out using

the Vienna ab initio simulation package (VASP) [43]. The generalized gradient approximation (GGA) was employed parameterized by Perdew-Burke-Ernzerhof (PBE) exchange-correlation functional [44]. Ionic cores were described by the projector augmented wave (PAW) method [45]. The wave functions were constructed from the expansion of planewaves with an energy cutoff of 400 eV. A  $1 \times 1 \times 1$  Monkhorst-Pack k-point mesh was used to sample the Brillouin zone. All calculations were converged until the forces on all atoms were less than 0.03 eV/Å. The electronic optimization steps were converged self-consistently to  $< 2 \times 10^{-5}$  eV. For the calculation of bulk optimization, the cut-off energy was increased to 520 eV and a  $6 \times 6 \times 4$  k-point mesh was used. The surface was constructed by cleaving the optimized bulk structure along the (101) surface of anatase TiO<sub>2</sub> and the (110) surface of rutile TiO<sub>2</sub>, which are the most abundant surface in the practical case. To prevent in-physical electronic interactions, 20 Å of the vacuum region between the slabs was added. Both (101) anatase TiO<sub>2</sub> and (110) rutile TiO<sub>2</sub> surfaces largely consisted of 3 layers and the top 2 layers were allowed to relax while the residual bottom layer was fixed. In the DOS calculations,  $2 \times 2 \times 1$  Gamma-Centered k-point mesh was used. DFT+U within Dudarev's approach was used with  $U_{\text{eff}}=3.5$  [46,47] to account for the on-site Coulomb interaction in the localized Ti 3d orbital.

## 2.3 Results and discussion

### 2.3.1 Physicochemical and optical property of 2 wt.% Au/TiO<sub>2</sub>

The physicochemical properties of prepared samples were proved by FE-SEM, HR-TEM, EDS, ICP-AES, N<sub>2</sub> adsorption-desorption curve, and XRD measurement (Figure 2-2 – 2-4 and Table 2-1 and 2-2). The coterminous sized Au nanoparticles (NPs) were evenly distributed on TiO<sub>2</sub> to exclude metal size effects in localized surface plasmon resonance (LSPR) (Figure 2-5 – 2-7). The Au NP size distribution is listed in Figure 2-6 where the overall average size of Au is in the range of 6.1 ~ 6.5 nm. The own characteristic crystal phases of TiO<sub>2</sub>s were determined by XRD measurement which were not changed by Au loading (Figure 2-8). Importantly, the crystallite size of anatase TiO<sub>2</sub> rods (RA<sub>na</sub>) and rutile TiO<sub>2</sub> rods (RR<sub>ut</sub>), as calculated using the Scherrer equation, is the same at 26 nm, which permits the precise analysis of the crystal phase effect. The crystallite size of rutile TiO<sub>2</sub> in RR<sub>ut</sub> or 3DR<sub>ut</sub> was also observed by HR-TEM with FFT analysis (Figure 2-9). The rutile TiO<sub>2</sub> crystallite with 30 nm by 17nm size was identified. The light absorption property of a series of TiO<sub>2</sub> and Au/TiO<sub>2</sub> heterostructures was measured by UV-Vis DRS (Figure 2-10 and 2-11). The peaks of TiO<sub>2</sub> (~400 nm) in Au loaded RR<sub>ut</sub> and 3D hierarchical rutile TiO<sub>2</sub> (3DR<sub>ut</sub>) were red shifted to a larger extent than the corresponding peaks in Au loaded small anatase TiO<sub>2</sub> spheres (SA<sub>na</sub>), large anatase TiO<sub>2</sub> spheres (LA<sub>na</sub>), and RA<sub>na</sub> due to the lower bandgap of pristine rutile TiO<sub>2</sub> than anatase TiO<sub>2</sub>. The peaks in all samples were slightly extended into the visible light region because of the formation of surface states in which

Au and TiO<sub>2</sub> are in contact [48]. The characteristics of the LSPR lifetime was identified from homogeneous LSPR linewidth in the region of visible light ( $\Gamma_{\text{hom}}$ ), which can be calculated from the intrinsic Fano analysis of  $F(R_{\infty})/\omega$  obtained from absorbance values of Au/TiO<sub>2</sub>s [49-51]. The LSPR lifetime is related to the LSPR dephasing time  $T_2$ , and  $T_2$  is a function of  $\Gamma_{\text{hom}}$  by the equation,  $T_2 = 2\hbar / \Gamma_{\text{hom}}$ . From the LSPR parts of Au/RRut and Au/3DRut spectra,  $\Gamma_{\text{hom}}$  was calculated to be 0.434 eV in Au/RRut, and 0.422 eV in Au/3DRut (see inset of Figure 2-10), which means that the LSPR lifetime of Au/3DRut is longer. The same result was observed between Au/SAna and Au/RAna. Thus, it can be concluded that the lifetime of hot electrons generated by LSPR phenomenon are affected by the morphology of TiO<sub>2</sub> and with the order of sphere < rod < 3D hierarchical structure.

### 2.3.2 Photocatalytic degradation of RNO

For a comparison of photocatalytic performance under visible light (>455 nm for exclusion of possibility of TiO<sub>2</sub> excitation, as 3.0 eV bandgap of rutile TiO<sub>2</sub> can absorb light up to 413 nm), RNO, which is known to be only degraded by hydroxyl radical, was used as a model organic compound (Figure 2-12). Hydroxyl radicals can be produced from both electron sites in TiO<sub>2</sub> CB and hole sites in Au NPs (Figure 2-13) [52]. The photocatalytic activities of Au/TiO<sub>2</sub> heterostructures were in the order of Au/SAna < Au/P 25 < Au/RAna < Au/LAna < Au/RRut < Au/3DRut. Generally, Au supported on rutile TiO<sub>2</sub>s showed a much better performance than Au supported on anatase TiO<sub>2</sub>s.

Regarding the effect of structure, the photodegradation rate of Au supported on the 3D hierarchical structure was faster than that for the rod form ( $\text{Au/RRut} < \text{Au/3DRut}$ ) and the Au supported on rod was faster than that for the sphere ( $\text{Au/SAna} < \text{Au/RAna}$ ), which corresponds to the LSPR lifetime (Figure 2-13). For the determination of relationship between  $\text{TiO}_2$  surface and photocatalytic activity, the difference of surface hydroxyl group generated by a series of  $\text{TiO}_2$ s were comparatively analyzed. In Figure 2-14, the FT-IR spectra of a series of  $\text{Au/TiO}_2$ s show broad band in the region of  $3550\text{-}3100\text{ cm}^{-1}$ , which stands for Ti-OH stretching modes [53-57]. The absorption of Ti-OH stretching mode of a series of  $\text{Au/TiO}_2$ s were in the order of  $\text{Au/RRut} \approx \text{Au/3DRut} < \text{Au/RAna} \approx \text{Au/LAna} < \text{Au/SAna}$ , which shows similar trend with BET surface areas of a series of  $\text{Au/TiO}_2$ s (Table 2-2). As the surface hydroxyl group of  $\text{TiO}_2$  can act as a charge trap site for the photocatalysis and enhances charge separation [58], the amount of the surface hydroxyl group is known to be the determining factor for photocatalytic activity when bare  $\text{TiO}_2$  is used as a photocatalyst. Thus, the photocatalytic activity tendency is expected to be  $\text{Au/RRut} \approx \text{Au/3DRut} < \text{Au/RAna} \approx \text{Au/LAna} < \text{Au/SAna}$  in the general semiconductor photocatalytic system. However, the actual plasmonic photocatalytic activity under visible light was the order of  $\text{Au/SAna} < \text{Au/P 25} < \text{Au/RAna} < \text{Au/LAna} < \text{Au/RRut} < \text{Au/3DRut}$ , which shows the reverse trend. Since charge separation occurs between Au and  $\text{TiO}_2$  CB in the plasmonic photocatalytic system, plasmonic interaction of Au NPs and interaction between Au and  $\text{TiO}_2$  can also be the major factors for improving photocatalytic activity.

### 2.3.3 Effect of morphology in rutile phase TiO<sub>2</sub>

The enhanced plasmonic interaction in Au/3DRut was observed by DFM. Since samples were prepared by drop casting on glass, there are a few aggregated parts. Thus, single particle which shows the same absorption spectrum with UV-Vis DRS were selected for the measurement of scattering spectra (Figure 2-15). After white light irradiation on a single particle, a substantial red shift in the LSPR peak and amplified plasmonic interaction in Au/3DRut were observed [59]. To verify the advantage of a 3D structure, plasmonic interaction of two Au NPs depending on the irradiated light angle was calculated by means of the FDTD simulation (Figure 2-16a). When the tilted angle is lower than 45°, the transverse mode becomes more dominant than the longitudinal mode and a blue shift with decreased intensity of electromagnetic (EM) field in the LSPR peak occurs. When the tilted angle is higher than 45°, the longitudinal mode is formed and the reverse phenomenon happens. It should be noted that transverse mode coupling severely obstructs the EM field amplification from the longitudinal mode coupling. Even when the tilted angle is 60° where the longitudinal mode is dominant, the power intensity is smaller than that from independent Au NP. However, when it reaches 90°, a dramatic increase in intensity of the EM field as well as red shift occurs. Rods from Au/RRut are randomly oriented in the photocatalytic system and plasmonic interaction effects in all angles are negatively averaged. On the other hand, rods in the Au/3DRut are oriented in an orderly manner and most of the Au NP array can be irradiated by light in the vertical direction. This

confined structure effect facilitates the strongly amplified longitudinal plasmonic interaction, which leads the LSPR peak of Au/3DRut becomes red-shift with high intensity (Figure 2-16b).

### **2.3.4 Interfacial charge transfer rate comparison in 2 wt.% Au/TiO<sub>2</sub> heterostructures**

TR-PL was conducted to quantitatively examine the hot electron transfer rate from Au NPs to TiO<sub>2</sub> CB using 500 nm excitation laser (Figure 2-17 and 2-18), which is correlated with the generation of hydroxyl radicals. Prior to the TR-PL measurement, characteristic PL emissions of a Rhodamine B (RhB) dye solution and an aqueous solution of TiO<sub>2</sub> were observed by steady-state photoluminescence (SS-PL) spectra (Figure 2-19). The maximum SS-PL of RhB was 580 nm with a 500 nm wavelength excitation and all of the TiO<sub>2</sub> and Au/TiO<sub>2</sub> samples exhibited a 580 nm wavelength emission as well. For the TR-PL analysis, all of the TiO<sub>2</sub> and Au/TiO<sub>2</sub> samples were dispersed in 1 μM RhB aqueous solution. Measured spectra were fitted to the sum of three exponential decay functions expressed as:

$$I(t) = \sum_{i=1}^n A_i e^{-\frac{t}{\tau_i}} \quad (1)$$

The emission of RhB was expressed by a one exponential function and that of TiO<sub>2</sub> also by a one exponential function. In the case of TiO<sub>2</sub> and Au/TiO<sub>2</sub> in the RhB solution, the derived parameters are listed in Table 2-3. As shown in the proposed scheme in Table 2-4, the governing equation can be expressed by two

exponential decay functions [60,61]. The relative electron transfer rate constants from Au to TiO<sub>2</sub> ( $k_{R \rightarrow A \rightarrow T}$ ) were calculated and included in Table 2-4. The  $k_{R \rightarrow A \rightarrow T}$  values of a series of Au/TiO<sub>2</sub> heterostructures are presented in Figure 2-17b and other electron transfer rate constants are listed in Table 2-5. It should be noted that the tendency of  $k_{R \rightarrow A \rightarrow T}$  corresponds to the photocatalytic activity in Figure 2-12. This indicates that a faster electron-hole formation in Au which is in junction with TiO<sub>2</sub> improved photocatalytic activity. It is noticeable that  $k_{R \rightarrow A \rightarrow T}$  of Au/RRut is about 2.9 times higher than that of Au/RAna in spite of their similar structure, crystallite size, and aspect ratio. Thus, the main reason for this difference can be attributed to a crystal phase effect.

The detail crystal phase effect was explored using DFT calculations. The binding energy ( $\Delta E$ ) of Au and DOS in the two crystal phases of Au/TiO<sub>2</sub>s were calculated. Especially, (101) plane for anatase and (110) plane for rutile were chosen based on the fact that the two planes are the most stable plane for each crystal phase, respectively [62,63]. The findings indicate that the binding energies of Au in almost all of the possible binding sites in (110) rutile TiO<sub>2</sub> are much stronger than those in (101) anatase TiO<sub>2</sub> (Table 2-6). For a more precise examination, the DOS of TiO<sub>2</sub> and Au/TiO<sub>2</sub> were calculated and compared. When Au is bonded with rutile TiO<sub>2</sub>, a  $\sim 0.294$  eV band shift was observed, while that for anatase TiO<sub>2</sub> was  $\sim 0.002$  eV which is negligible. This difference can be related to the extent of the contribution of Au DOS to each of the TiO<sub>2</sub> crystal phase. In the case of Au/anatase TiO<sub>2</sub>, Au DOS mainly exists below the Fermi level and is totally included in the anatase TiO<sub>2</sub> VB. On the other hand,

in the case of Au/rutile TiO<sub>2</sub>, Au DOS partially exists above the Fermi level and is, in part, included to the rutile TiO<sub>2</sub> CB. This suggests that totally different hot electron transfer paths can exist for the two TiO<sub>2</sub> crystal phases. At the Au and anatase TiO<sub>2</sub> interface, hot electrons generated by LSPR can only transfer to anatase TiO<sub>2</sub> by electron tunneling effect since there are no Au states in anatase TiO<sub>2</sub> CB. However, at the interface between Au and rutile TiO<sub>2</sub> CB, a direct, hot electron transfer is possible in the presence of Au DOS in rutile TiO<sub>2</sub> CB. Therefore, the amount of transferred electrons between Au and rutile TiO<sub>2</sub> should be much more than that for anatase TiO<sub>2</sub> by efficient electron transfer aided by the stronger and closer binding of Au with rutile TiO<sub>2</sub>.

### **2.3.5 Discussion of different energy band diagram between Au/anatase TiO<sub>2</sub> and Au/rutile TiO<sub>2</sub>**

Here, the Schottky barrier ( $\phi_{SB}$ ) is not the determining factor for  $k_{R \rightarrow A \rightarrow T}$ . As hot electrons generated by LSPR have a sufficient energy of 2.48 eV which is much higher than the  $E_F$  of Au to overpass the barrier. However, considering the reverse directional electron transfer path (TiO<sub>2</sub>→Au), the Schottky barrier ( $\phi_{SB}$ ) or the potential of band bending ( $V_{BB}$ ) needs to be considered. For example, according to the RNO photodegradation data (Figure 2-12) and the TR-PL spectra (Figure 2-17), Au/LAna showed a better photocatalytic activity and a higher  $k_{R \rightarrow A \rightarrow T}$  than Au/SAna in spite of their same crystal phase. These results can be attributed to the excessively small size of SAna that precludes it from forming a depletion layer (D) or a space charge region [64]. The

calculation indicates that the  $V_{BB}$  of  $TiO_2$  is only  $\sim 0.004$  V when the particle radius equals to the Debye length ( $L_D$ , 3.8 – 12 nm, with  $\epsilon_r \approx 100$  and  $N_d \approx 10^{24} - 10^{25} \text{ m}^{-3}$ ) as following equation [65]:

$$V_{BB} = \frac{eN_d D^2}{2\epsilon_r \epsilon_0} \quad (2)$$

A Au/SAna heterostructure would cause an incomplete depletion layer and a low  $V_{BB}$ , which enables the easy overpass of electrons from  $TiO_2$  CB to Au, resulting in a fast electron-hole recombination on Au. Likewise, this phenomenon is identically applied to the crystal phase effect. As discussed above, significant band shift ( $\sim 0.294$  eV) in Au/rutile  $TiO_2$  induces a larger  $V_{BB}$  which results in slower electron-hole recombination.

A proposed electron transfer process for the two types of Au/ $TiO_2$  under visible light is presented in Figure 2-20 based on above results. Stronger and closer binding is formed between Au and rutile  $TiO_2$ , which enables electrons to flow from Au to rutile  $TiO_2$  more easily than in case of anatase  $TiO_2$ . It was once considered that the CB minimum in anatase  $TiO_2$  is  $\sim 0.2$  eV higher than rutile  $TiO_2$ . However, an opposite view has arisen to be fact in the recent studies, which supports the conclusion that the CB minimum in rutile  $TiO_2$  is  $\sim 0.2$  eV higher than anatase  $TiO_2$  [66,67]. Hence, both  $\phi_{SB}$  and  $V_{BB}$  would be expected to be higher in the Au/rutile  $TiO_2$  system. Furthermore, due to the higher band shift in Au/rutile  $TiO_2$  observed in DFT calculations,  $V_{BB}$  becomes higher which delays electron-hole recombination. Therefore, it can be concluded that more electrons are transferred from Au to rutile  $TiO_2$  and less electrons are transferred from rutile  $TiO_2$  to Au than in case of anatase  $TiO_2$ .

**Table 2-1.** The final content of Au in a series of Au/TiO<sub>2</sub> samples calculated from ICP-AES.

Sample	Au content (%)
Au/SA <sub>na</sub>	2.62
Au/LA <sub>na</sub>	2.33
Au/RA <sub>na</sub>	2.48
Au/RR <sub>ut</sub>	2.63
Au/3DR <sub>ut</sub>	2.44

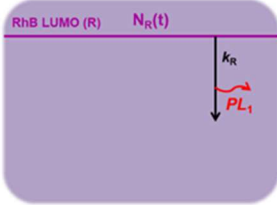
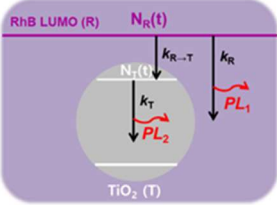
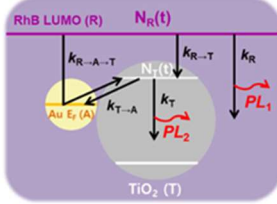
**Table 2-2.** BET surface area, pore volume, and average pore diameter of the synthesized 2 wt.% Au/TiO<sub>2</sub> heterostructures.

Sample	BET surface area (m <sup>2</sup> g <sup>-1</sup> )	Pore volume (cm <sup>3</sup> g <sup>-1</sup> )	Average pore diameter (nm)
Au/SAAna	70.93	0.3339	18.83
Au/LAna	31.56	0.2028	25.71
Au/RAna	41.66	0.2846	27.32
Au/P 25	49.92	0.2817	22.57
Au/RRut	13.17	0.06585	20.00
Au/3DRut	10.88	0.04525	16.63

**Table 2-3.** Kinetic parameters extracted from fitted results of time-resolved PL spectra.

In RhB Solution	A <sub>1</sub>	$\tau_1$ (ns)	A <sub>2</sub>	$\tau_2$ (ns)	$\chi^2$
None	4728.2	1.7722			0.9558
SAna	404.4	2.617	6003.3	1.6775	0.9658
Au/SAna	425.6	2.405	5507.8	1.6669	0.9703
LAna	371.3	2.722	6342.3	1.6696	1.0066
Au/LAna	409.5	2.555	5396.9	1.638	0.9807
ARut	396.4	2.847	6194.4	1.6877	0.9939
Au/RAna	424.1	2.613	4814.1	1.6637	1.0181
RRut	526.7	2.636	7349.9	1.705	1.0443
Au/RRut	513.2	2.493	5136.7	1.6366	1.0175
3DRut	570.9	2.519	6972.4	1.7037	0.9576
Au/3DRut	612.3	2.372	4986.4	1.6155	0.9918

**Table 2-4.** Electron transfer paths, governing equations, and analytical solutions in a RhB solution, TiO<sub>2</sub> in a RhB solution, and Au/TiO<sub>2</sub> in a RhB solution with an excitation wavelength of 500 nm.

Electron transfer path	Governing equation and analytic solution
	(i) $\frac{dN_R}{dt} = -k_R N_R$ $\rightarrow N_R = N_{R0} e^{-k_R t}$
	(i) $\frac{dN_R}{dt} = -(k_R + k_{R-T}) N_R$ $\rightarrow N_R = N_{R0} e^{-(k_R + k_{R-T}) t}$ (ii) $\frac{dN_T}{dt} = k_{R-T} N_R - k_T N_T$ $\rightarrow N_T = A_1 e^{-(k_R + k_{R-T}) t} + A_2 e^{-k_T t}$
	(i) $\frac{dN_R}{dt} = -(k_R + k_{R-T} + k_{R-A-T}) N_R$ $\rightarrow N_R = N_{R0} e^{-(k_R + k_{R-T} + k_{R-A-T}) t}$ (ii) $\frac{dN_T}{dt} = (k_{R-T} + k_{R-A-T}) N_R - (k_T + k_{T-A}) N_T$ $\rightarrow N_T = A_3 e^{-(k_R + k_{R-T} + k_{R-A-T}) t} + A_4 e^{-(k_T + k_{T-A}) t}$

\* The method of calculating electron transfer rate constants from kinetic parameters is presented below.

$$[1] \quad k_R = \frac{1}{\tau_{1, None}}$$

$$[2] \quad k_{R \rightarrow T} = (k_{R \rightarrow T} + k_R) - k_R = \frac{1}{\tau_{1, TiO_2}} - \frac{1}{\tau_{1, None}}, \quad k_T = \frac{1}{\tau_{2, TiO_2}}$$

$$[3] \quad k_{R \rightarrow A \rightarrow T} = (k_{R \rightarrow A \rightarrow T} + k_{R \rightarrow T} + k_R) - (k_{R \rightarrow T} + k_R)$$

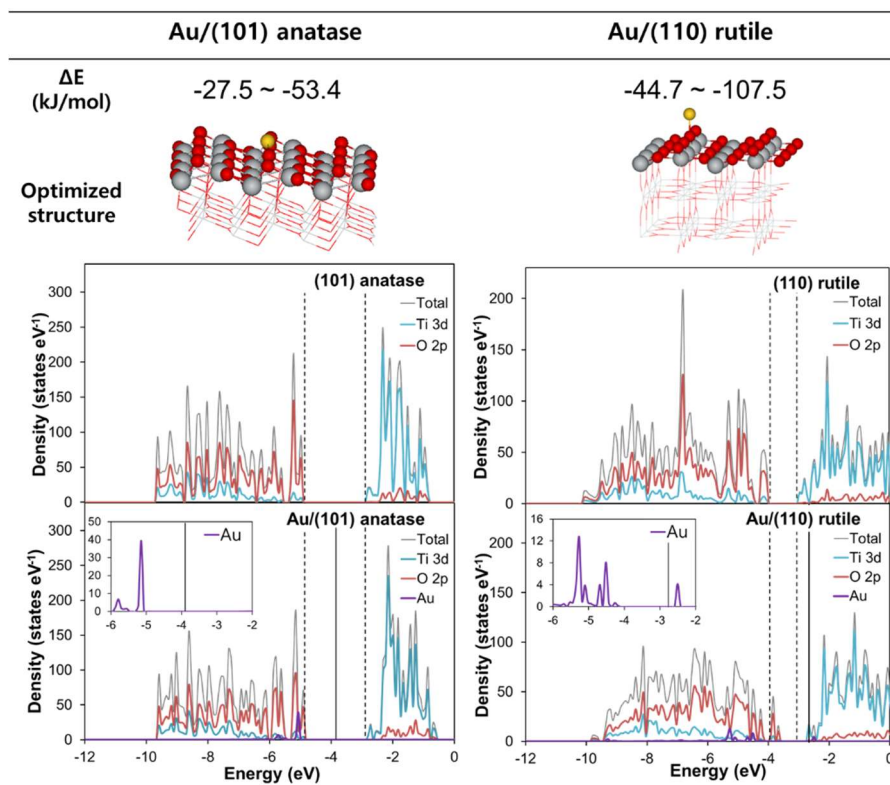
$$= \frac{1}{\tau_{1, Au/TiO_2}} - \frac{1}{\tau_{1, TiO_2}},$$

$$k_{T \rightarrow A} = (k_{T \rightarrow A} + k_T) - k_T = \frac{1}{\tau_{2, Au/TiO_2}} - \frac{1}{\tau_{2, TiO_2}}$$

**Table 2-5.** Electron transfer rate constants of Au/TiO<sub>2</sub> in the presence of RhB. The kinetic parameters were extracted from the fitted results of time-resolved PL spectra (Table 2-3), and electron transfer rate constants were calculated by electron transfer paths described in Table 2-4.

( $\times 10^8 \text{ s}^{-1}$ )	$k_R$	$k_{R \rightarrow T}$	$k_{R \rightarrow A \rightarrow T}$	$k_T$	$k_{T \rightarrow A}$
Au/SAna		0.319	0.038	3.821	0.337
Au/LAna		0.347	0.116	3.674	0.240
Au/RAna	5.643	0.283	0.085	3.512	0.315
Au/RRut		0.222	0.245	3.794	0.218
Au/3DRut		0.227	0.320	3.970	0.246

**Table 2-6.** DFT calculation results for Au/anatase and Au/rutile. Binding energies of every possible sites, the most stable structure, and DOS spectra coming from those structures are listed. In the DOS spectra, dashed lines indicate CB minimum and VB maximum of TiO<sub>2</sub>, and continuous lines indicate E<sub>F</sub> of Au/TiO<sub>2</sub>. E<sub>F</sub> of TiO<sub>2</sub> matches with VB maximum line.



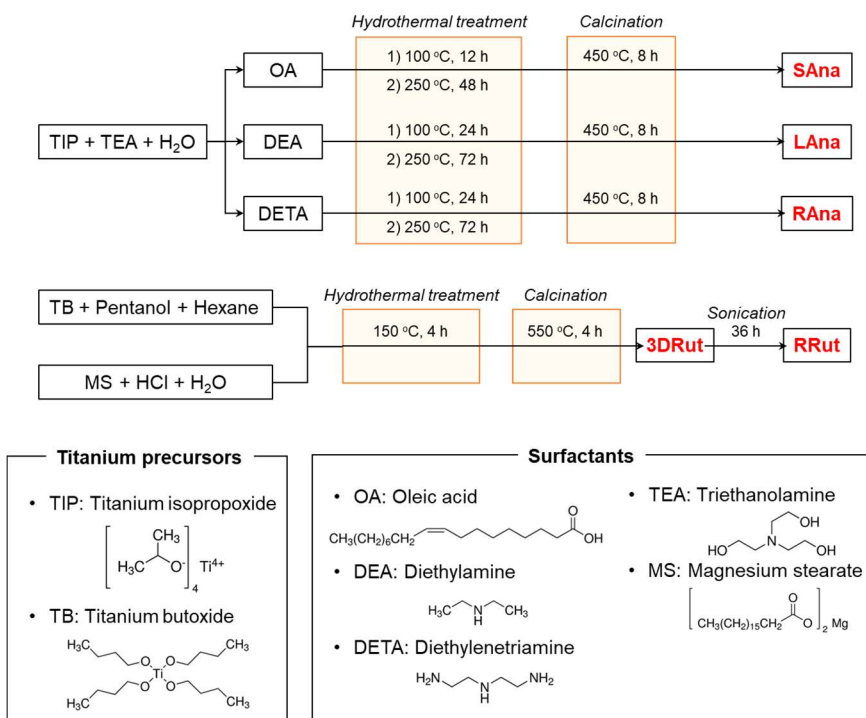


**Figure 2-1.** Schematic diagram for the preparing methods of a series of  $\text{TiO}_2$  samples.

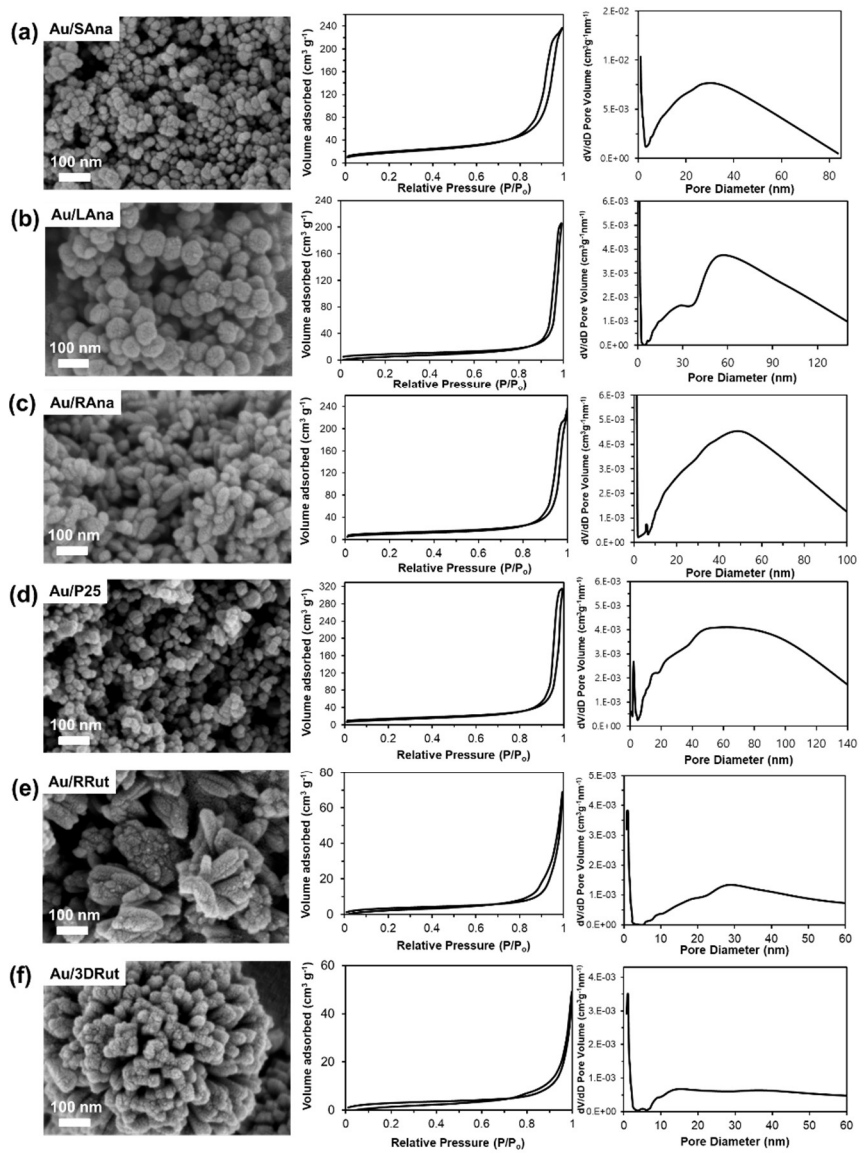


**Figure 2-2.** FE-SEM image,  $N_2$  adsorption-desorption isotherm, and pore size distribution for (a) Au/SAna, (b) Au/LAna, (c) Au/RAna, (d) Au/P25, (e) Au/RRut, and (f) Au/3DRut.

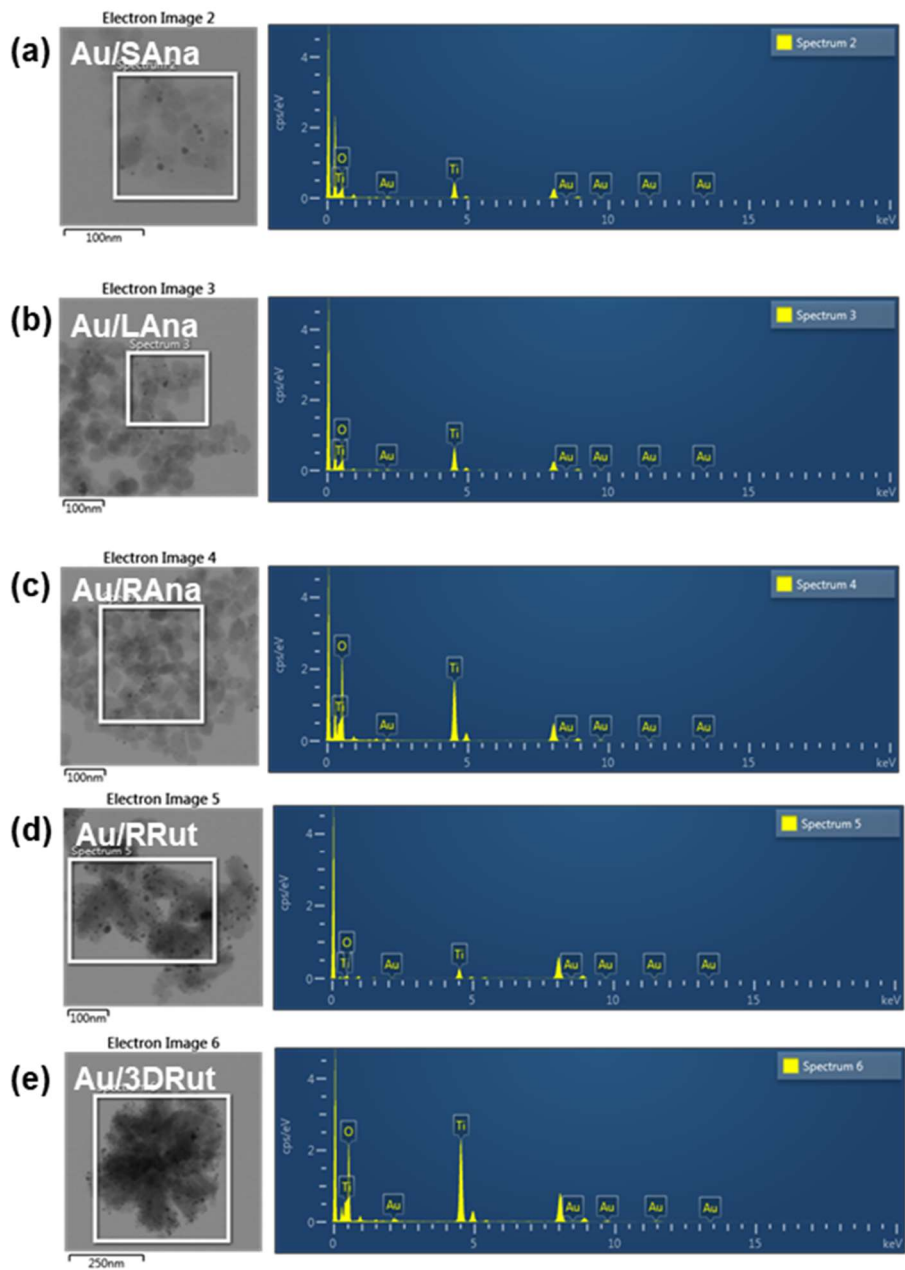


**Figure 2-3.** EDS spectra of a series of Au/TiO<sub>2</sub> samples. (a) Au/SAna, (b) Au/LAna, (c) Au/RAna, (d) Au/RRut, and (e) Au/3DRut.

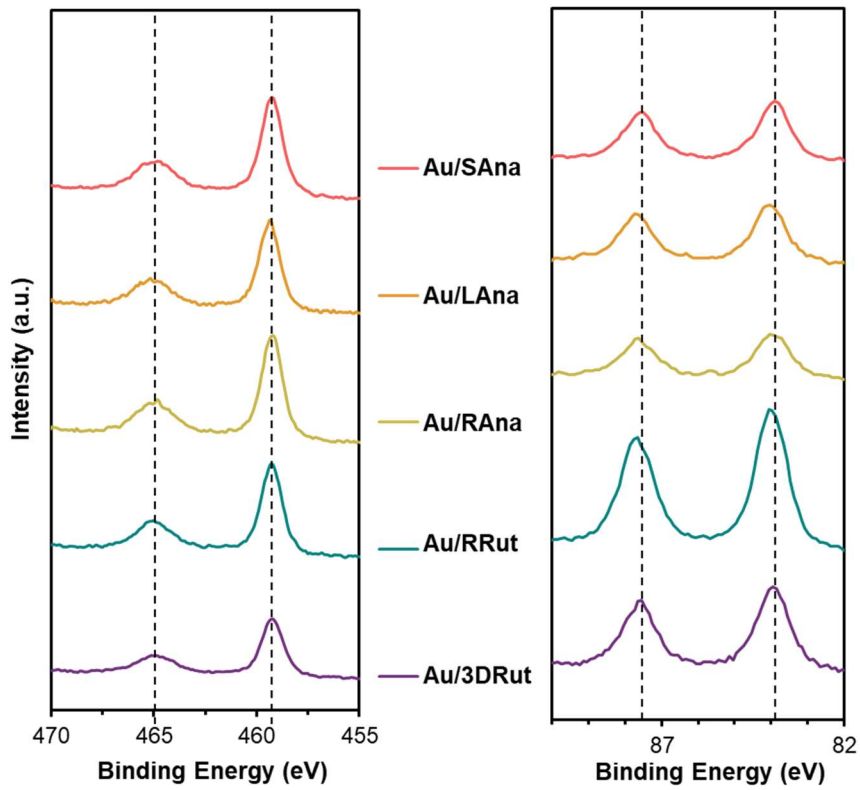


**Figure 2-4.** X-ray photoemission spectra of a series of Au/TiO<sub>2</sub> samples. In the ranges of Au 4f and Ti 2p were observed.

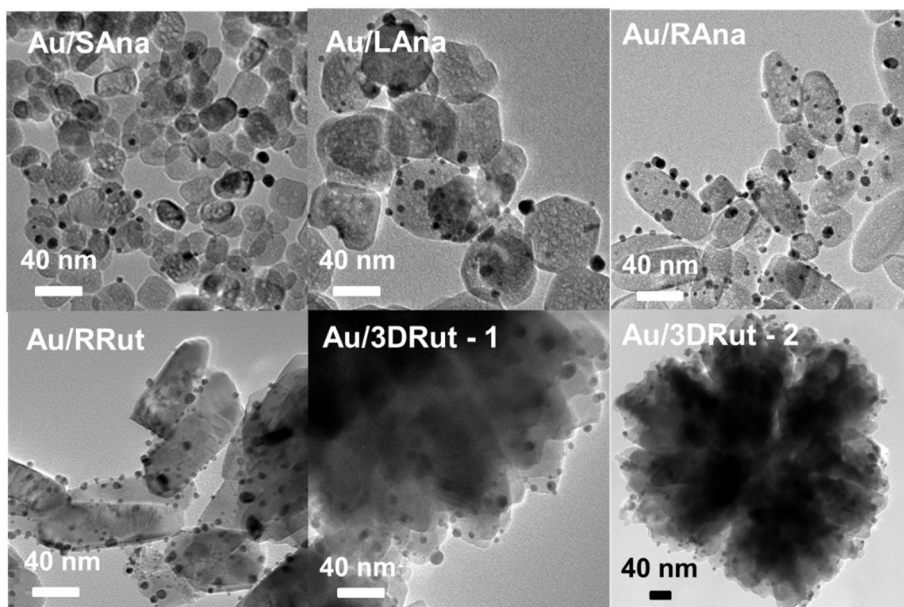


**Figure 2-5.** HR-TEM images of a series of 2 wt.% Au/TiO<sub>2</sub> heterostructures. Au/3DRut-1: High-magnified image and Au/3DRut-2: low magnified image, (SAna: small anatase TiO<sub>2</sub> spheres, BAAna: large anatase TiO<sub>2</sub> spheres, RAna: anatase TiO<sub>2</sub> rods, RRut: rutile TiO<sub>2</sub> rods, and 3DRut: 3D hierarchical rutile TiO<sub>2</sub>).

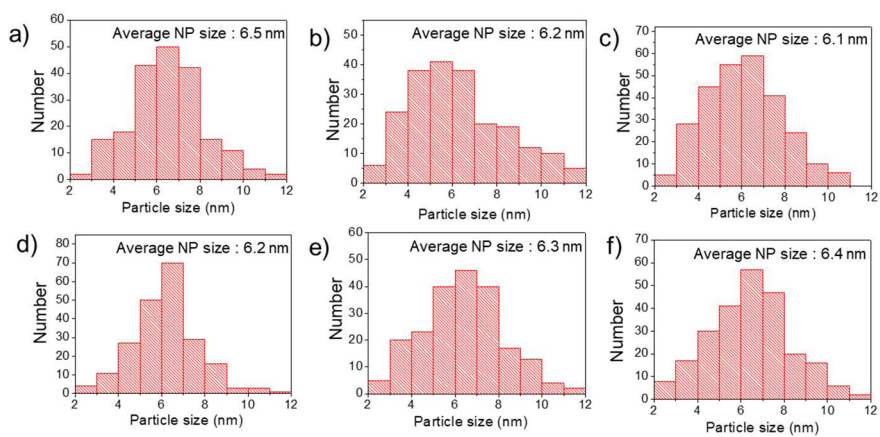


**Figure 2-6.** Au size distribution for (a) Au/SAna, (b) Au/LAna, (c) Au/RAna, (d) Au/P 25, (e) Au/RRut, and (f) Au/3DRut.

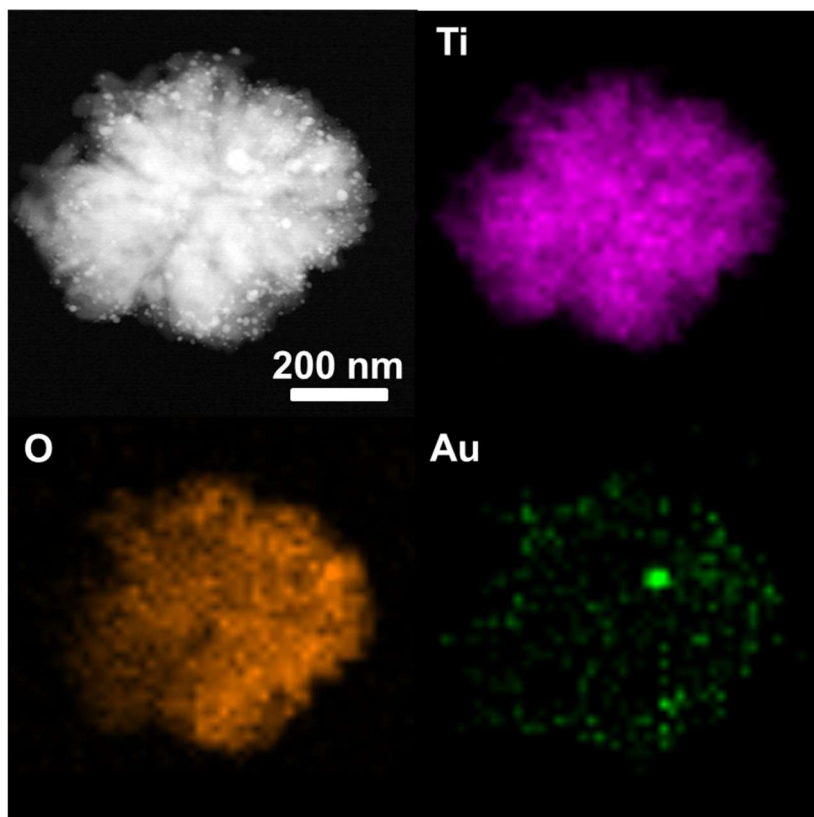


**Figure 2-7.** HADF-STEM images of 2 wt.% Au/3DRut. 2D atom mappings of Ti, O, and Au were conducted and are noted.

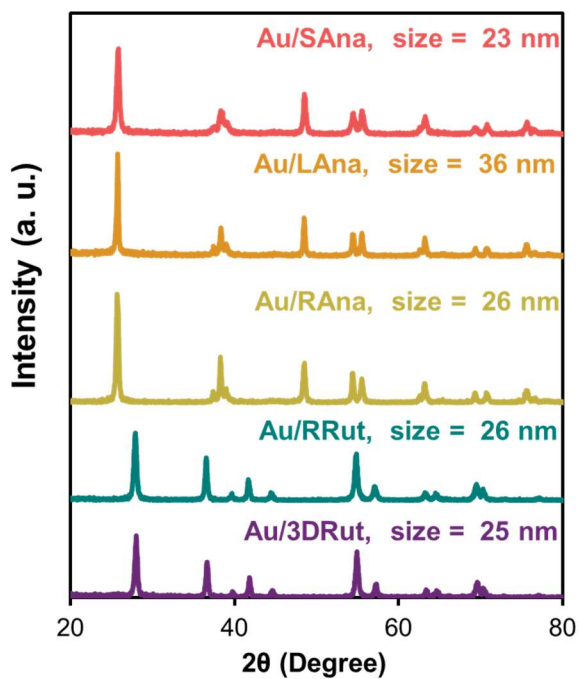


**Figure 2-8.** XRD spectra with calculated  $\text{TiO}_2$  crystallite sizes of a series of 2 wt.% Au/ $\text{TiO}_2$  heterostructures. In the absorption part of LSPR, units of axis were converged for calculations of LSPR linewidth and indicated inset.

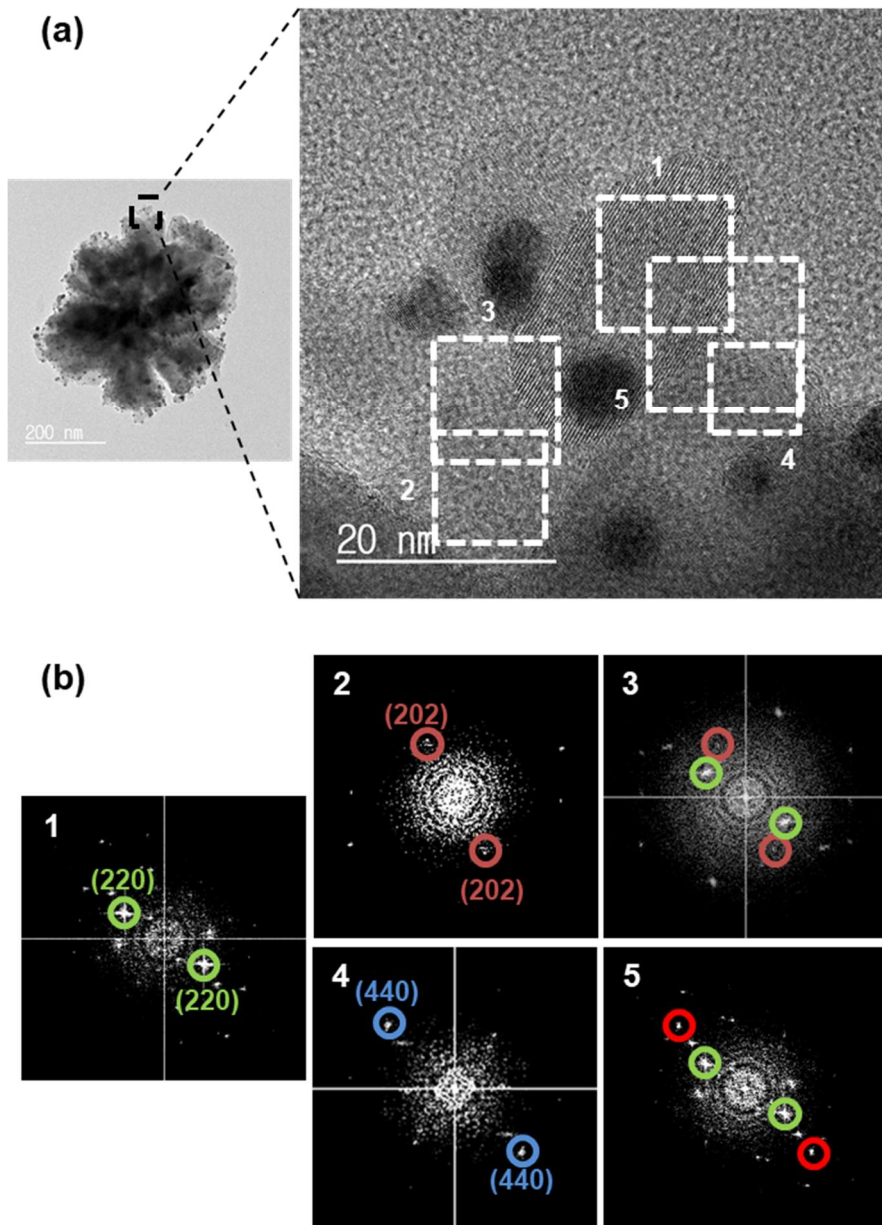


**Figure 2-9.** (a) HR-TEM images of Au/3DRut. The image was firstly obtained in 200 nm scale and magnified to 20 nm scale for the identification of rutile crystallite. (b) FFT patterns obtained from the magnified HR-TEM image.

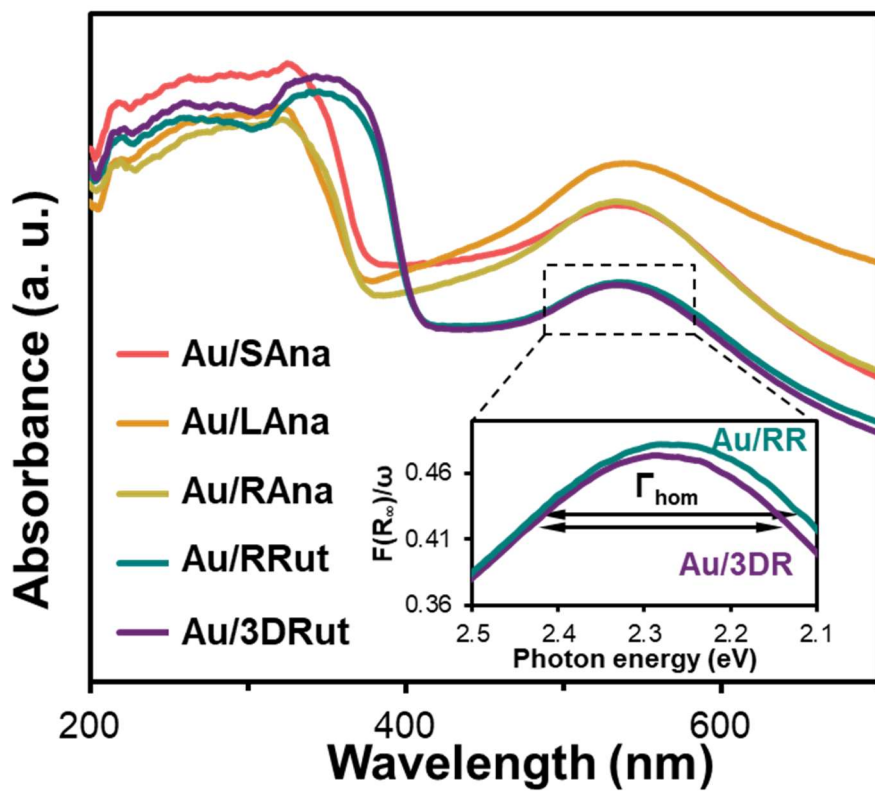


**Figure 2-10.** UV-Vis DRS spectra of a series of 2 wt.% Au/TiO<sub>2</sub> heterostructures. In the absorption part of LSPR, units of axis were converged for calculations of LSPR linewidth and indicated inset.

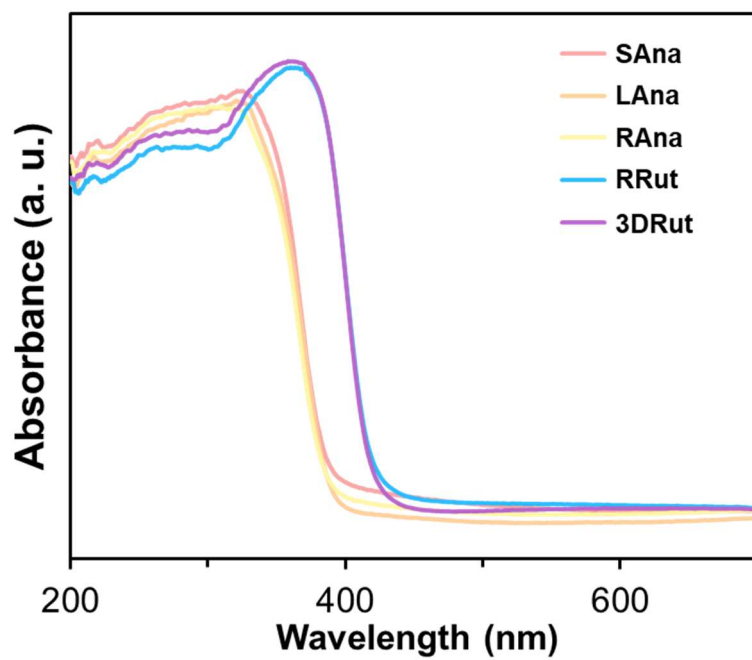


**Figure 2-11.** UV-Vis DRS spectra of a series of TiO<sub>2</sub> samples.

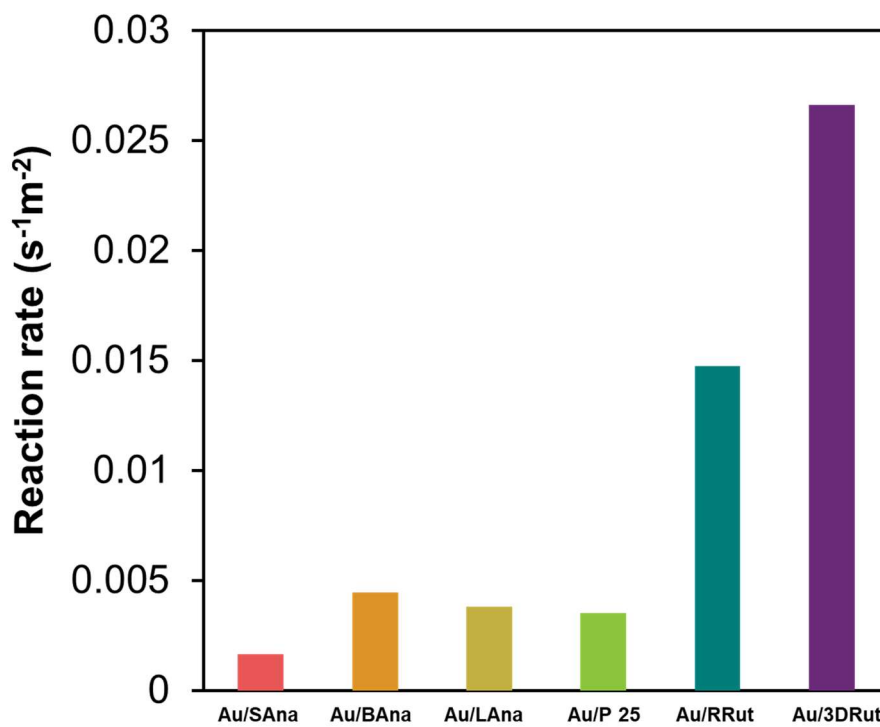


**Figure 2-12.** Photocatalytic degradation of RNO in the presence of a series of 2 wt.% Au/TiO<sub>2</sub> heterostructures under visible light (>455 nm filter).

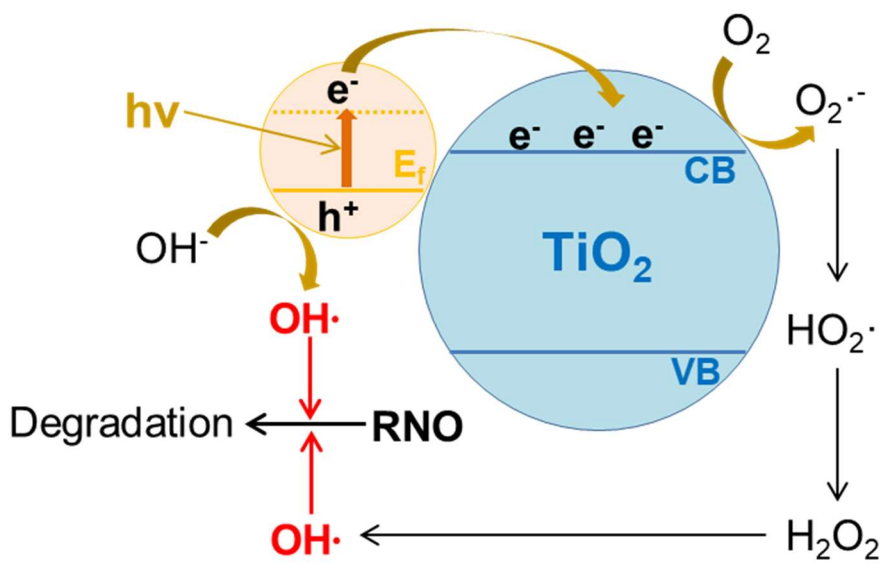


**Figure 2-13.** Hydroxyl radical formation path in Au/TiO<sub>2</sub> under visible light.

RNO is degraded by hydroxyl radical.

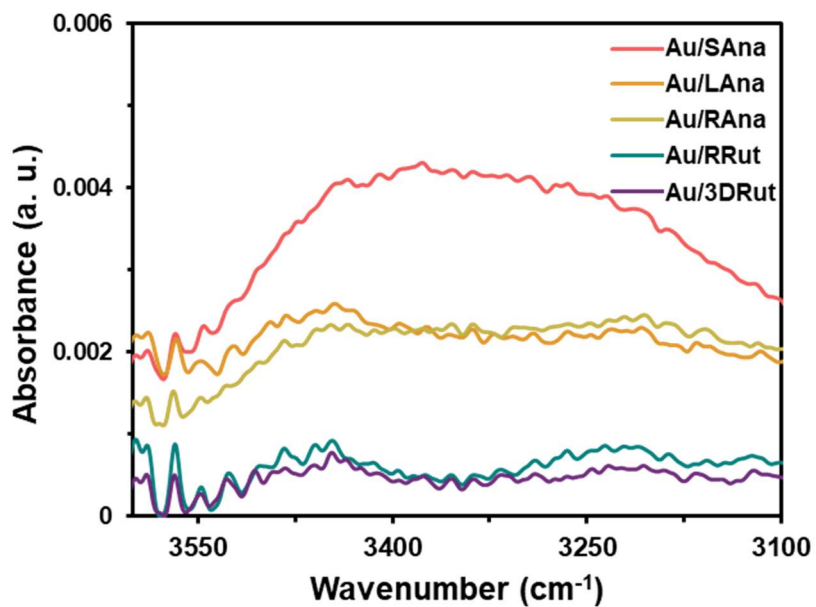


**Figure 2-14.** FT-IR spectra of a series of Au/TiO<sub>2</sub> samples. FT-IR spectra in the range of 3600-3100 cm<sup>-1</sup> represents surface hydroxyl group.

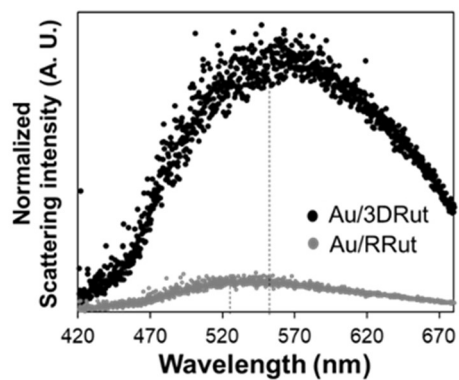


**Figure 2-15.** Dark-field scattering spectra of Au/3DRut and Au/RRut, which were obtained from dark field images and normalized with BET surface area.

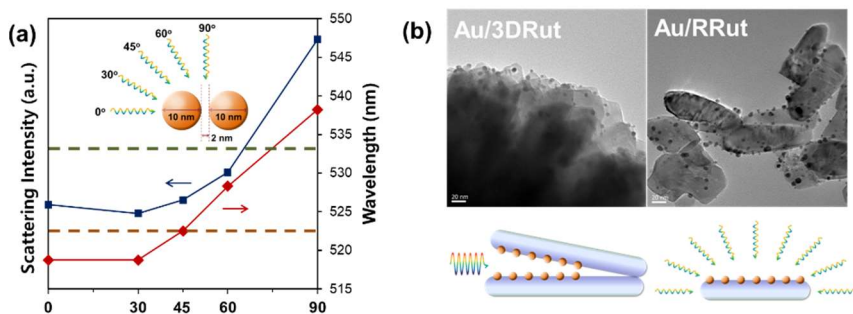


**Figure 2-16.** (a) FDTD simulations were performed according to inset scheme of coupled Au NPs with light irradiation in different directions. Derived wavelength and intensity were presented, and the values of original 10 nm Au NP were indicated by dotted lines. (b) TEM images of Au/3DRut and Au/RRut are listed above. Simplified schemes of Au/3DRut and Au/RRut including light irradiation are contained below.

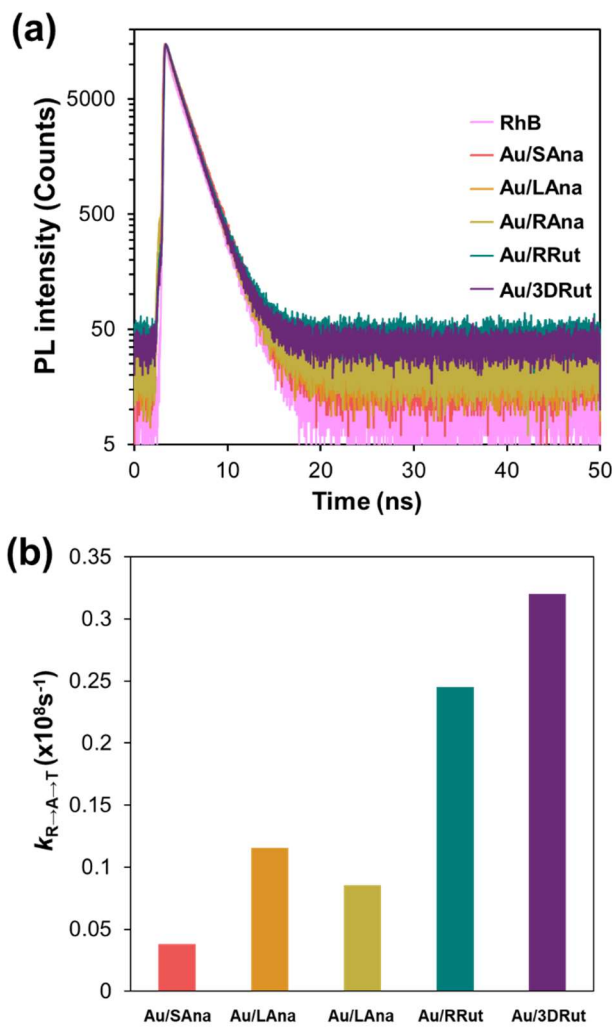


**Figure 2-17.** (a) TR-PL spectra of Au/TiO<sub>2</sub> in RhB solution. (b)  $k_{R \rightarrow A \rightarrow T}$  values of a series of Au/TiO<sub>2</sub> heterostructures. The values were derived from parameters obtained from TR-PL spectra.

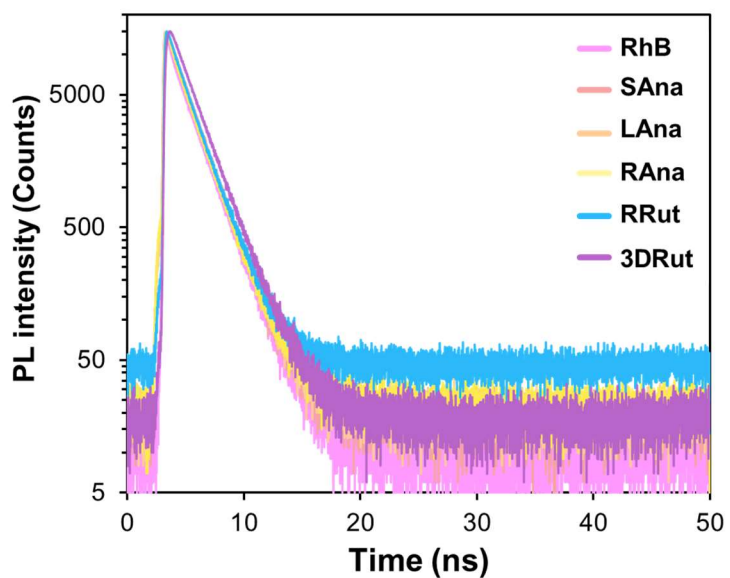


**Figure 2-18.** Time-resolved PL spectra of TiO<sub>2</sub> in the presence of 1  $\mu$ M RhB solution. All fitting parameters are described and summarized in Table 2-3.

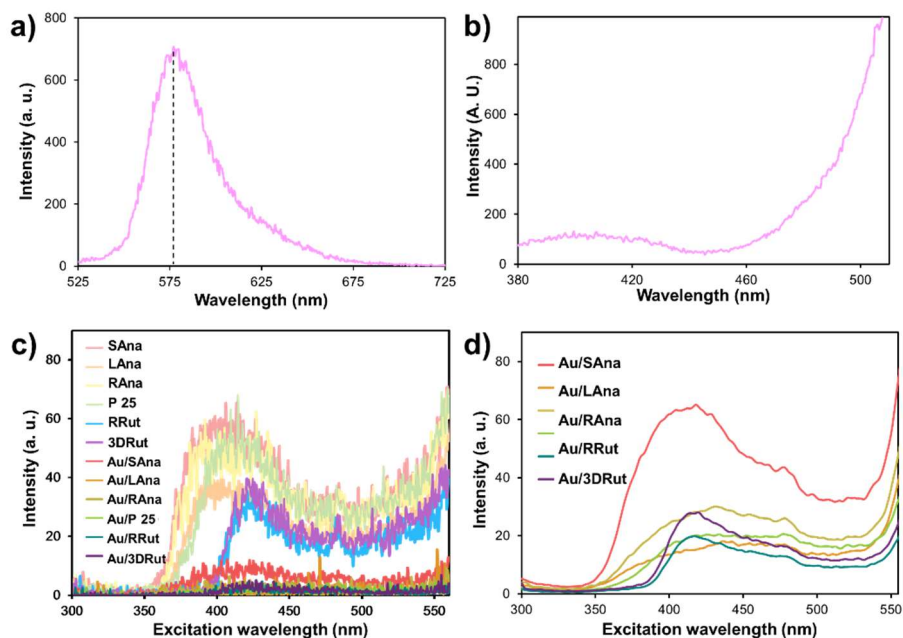


**Figure 2-19.** (a), (b) Steady-state PL (SSPL) spectra of a 1  $\mu\text{M}$  RhB solution measured in the emission mode at an excitation wavelength of 500 nm and the excitation mode at an emission wavelength of 580 nm. (c) SSPL spectra of a series of  $\text{TiO}_2$  heterostructures and Au/ $\text{TiO}_2$  in D.I. water measured with excitation mode at 580 nm emission wavelength. 2.5 nm slit was used for the measurements. (d) SSPL spectra of a series of Au/ $\text{TiO}_2$  heterostructures in D.I. water. To magnify emission spectra at 580 nm, 10 nm slit was used for the measurement.

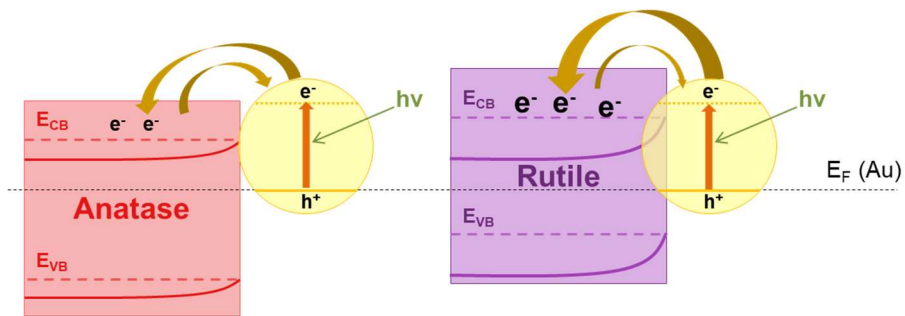


**Figure 2-20.** Schematic energy band diagram of two types of Au/TiO<sub>2</sub>, showing the proposed electron transfer processes under visible light.

# **Chapter 3. Modulating energetic alignment of Pt-TiO<sub>2</sub> system for enhanced charge separation directly related to a photocatalytic performance**

## **3.1 Introduction**

A positively charged state of metal results from charge separation at the M-S interface that occurs as follows. i) When semiconductors are excited by a mild light source. If a high Schottky barrier against electrons exists between the M-S interfaces, only holes can transfer from a semiconductor to metal. The high Schottky barrier could effectively block the transfer of weakly excited electrons from the semiconductor conduction band (CB) to metal, while that M-S contact produces a high electric field in the semiconductor valence band (VB) which enables the fast movement of a hole carrier. ii) When metal is excited by an external light source, interband transition could cause the induction of a positively charged state of general metal elements [68-71], although hot electron formation by local surface plasmon resonance (LSPR) [72,73] is the generally accepted process acting on mainly group IB metal elements. According to the above criteria, the Pt/rutile TiO<sub>2</sub> system could be operated as a synergetic charge separable system, which accumulates positive charge on metal cocatalyst parts under visible light. In the Pt/rutile TiO<sub>2</sub> system, a Schottky barrier with a height of more than 1 eV is formed as the result of

significant differences between the Fermi level of Pt (~5.6 eV) and rutile TiO<sub>2</sub> (~4.2 eV) [74]. When visible light ( $\lambda > 400$  nm,  $< 3.1$  eV) is irradiated to rutile TiO<sub>2</sub>, hole transfer from the semiconductor VB to metal is the only possible route. The 3.0 eV band gap of rutile TiO<sub>2</sub> allows partial absorption of visible light and excited electrons at the semiconductor CB have max surplus energies of approximately 0.1 eV. Thus, an electron transfer from the semiconductor CB to metal is unfavorable due to the Schottky barrier of more than 1 eV height. In the case of metal, on the other hand, excited electrons could be formed by interband transition and transfer from metal to the semiconductor CB, since those carriers have sufficient energy to overcome the Schottky barrier [75]. Therefore, the synergetic processes, which contains excited electron transfer from metal to the semiconductor CB and hole transfer from the semiconductor VB to metal, is expected for the charge separation in the Pt/rutile TiO<sub>2</sub> photocatalytic system under visible light.

In this study, the Pt/rutile TiO<sub>2</sub> material was adopted as a typical synergetic charge separable M-S photocatalytic system. The charge separation in the M-S interface was regulated by differentiation of M-S energetic alignment and band bending extent, which could come from the modulation of metal nanoparticle size and Fermi level. When the charge-transfer path between the Pt-TiO<sub>2</sub> interface was analyzed, the Pt was placed in a positively charged state by an integrated mechanism that included an electron transfer from Pt to the TiO<sub>2</sub> CB, and a hole transfer from the TiO<sub>2</sub> VB to Pt. Charge separation amount and rates were simultaneously increased or decreased in accordance with the differentiation of M-S energetic alignment. In order to observe the correlation

between the extent and rate of the positive charge accumulation on Pt and the practical photocatalytic activities, an acetaldehyde photodegradation reaction was conducted in the form of a gaseous oxidation reaction. This verified that a photocatalyst that contains a more positively charged metal by faster synergetic charge separation should also have a significantly increased oxidation reaction rate.

## 3.2 Experimental

### 3.2.1 Synthesis of Pt/TiO<sub>2</sub> photocatalysts with various Pt sizes

A series of Pt/TiO<sub>2</sub> photocatalysts with various sizes of Pt nanoparticles (NPs) were prepared by loading the Pt nanoparticles onto commercialized rutile TiO<sub>2</sub> supports (MT-500B, TAYCA). Chloroplatinic acid ( $\text{H}_2\text{PtCl}_6 \cdot 6\text{H}_2\text{O} \geq 99.9\%$ , Sigma-Aldrich) was utilized as the metal precursor. Sodium borohydride ( $\text{NaBH}_4$ , Sigma-Aldrich) was used as the reducing agent. All chemicals were used without further purification. The Pt/TiO<sub>2</sub> catalysts were obtained by a well-known chemical reduction method controlling the pH and temperature. The pH and the temperature were tailored in opposite directions to control the size of the Pt NPs. Electrostatic force was considered for the synthesis of desired size of Pt NPs. To obtain smaller Pt NPs,  $\text{PtCl}_6^{2-}$  anions were dispersed to a negatively charged TiO<sub>2</sub> surface, which was obtained under higher pH conditions. Synthesis temperature should be decreased for higher pH conditions to avoid non-uniform growth on the TiO<sub>2</sub> surface and nucleation in the liquid phase. The pH was controlled to 5, 3, and 1 via NaOH or HNO<sub>3</sub> solutions, and temperatures were maintained at 10 °C, 50 °C, and 60 °C, respectively, for the preparation of Pt(1.7)/TiO<sub>2</sub>, Pt(3.3)/TiO<sub>2</sub>, and Pt(5.1)/TiO<sub>2</sub>. 0.5 g TiO<sub>2</sub> powders and  $\text{H}_2\text{PtCl}_6 \cdot 6\text{H}_2\text{O}$  precursor solution were dispersed in 150 mL of deionized water by sonication for 30 min. Pt/TiO<sub>2</sub> was reduced by adding 0.02 M NaBH<sub>4</sub> solution dropwise to the aqueous batches, resulting in the deposition of 1 wt% Pt nanoparticles on a TiO<sub>2</sub> surface after stirring for 3 h. Finally, gray powders

were obtained after centrifugation, washed several times with D.I. water, and dried overnight at 60 °C. In order to remove the residual materials and to minimize the oxidized species of Pt, samples were thermally annealed at 300 °C for 3 h in the presence of a 10% H<sub>2</sub>/Ar flow.

### **3.2.2 Characterization**

The morphology and size of the synthesized Pt/TiO<sub>2</sub> were characterized by transmission electron microscopy (TEM, JEM-2100, JEOL, 200 kV) and Cs-TEM images were obtained by a cold field emission gun (Cs-TEM, JEM-ARM200F, JEOL, 200 kV). The final contents of deposited Pt in the Pt/TiO<sub>2</sub> catalysts were determined by inductively coupled plasma-atomic emission spectroscopy (ICP-AES, OPTIMA 4300DV, Perkin-Elmer). Ultraviolet-visible diffuse reflectance spectroscopy (UV-Vis-DRS, V670, JASCO) measurement was conducted to obtain UV-Vis spectra of the samples, using BaSO<sub>4</sub> as the reference. Crystallinity of the resulting samples was analyzed by X-ray diffraction spectroscopy (XRD, D/max-2500/PC, Rigaku) using Cu K $\alpha$  radiation ( $\lambda = 0.154$  nm) as the incident beam at 50 kV and 100 mA. The elemental chemical status was investigated by X-ray photoelectron spectroscopy (XPS, AXIS-His, KRATOS). Total surface areas of Pt/TiO<sub>2</sub>s were calculated by N<sub>2</sub> absorption using multipoint BET analysis (Micromeritics, ASAP-2010). CO chemisorption experiments were performed in a Micromeritics Autochem II chemisorption analyzer in order to determine the dispersion and specific surface area of the Pt NPs. The samples were reduced

at 300 °C under a H<sub>2</sub> flow for 3 h before analysis. Pt L<sub>3</sub> edge X-ray adsorption near edge spectra (XANES) analysis was conducted in a transmittance mode on a 10C wide XAFS beamline at the Pohang Light Source (PLS) at the 3.0 GeV storage ring with a beam current of ~300 mA. A reference Pt foil was measured for calibration of the samples. The XANES analysis was carried under light on/off conditions and spectra were obtained, which were renormalized using the ATHENA software program.

### **3.2.3 Electrochemical characterization**

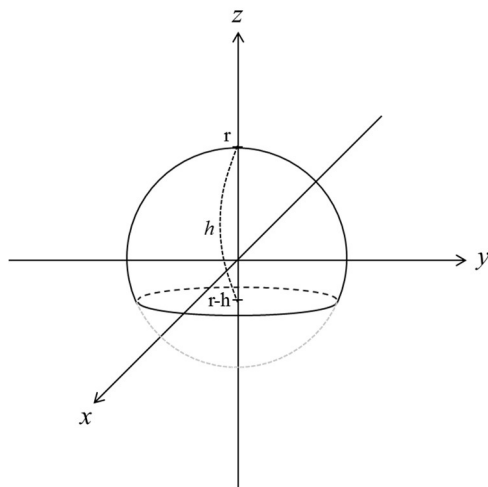
All electrochemical measurements were performed using a standard three-electrode cell. A platinum mesh was used as the counter electrode and an Ag/AgCl electrode served as the reference electrode. Electrochemical impedance spectroscopy (EIS) measurements were performed on the computer-controlled potentiostat (ZIVE SP2, WonATech). Pt/TiO<sub>2</sub> paste was deposited on FTO glass to form a film using the doctor blading method. 0.1 g sample was mixed with 0.01 g polyethylene glycol (Fluka), 0.01 g polyethylene oxide (Aldrich), 100 µL of acetylacetone ( $\geq$  99%, Sigma-Aldrich), and deionized water. The mixed slurry was bladed onto a 1 x 1 cm<sup>2</sup> area on FTO glass. The resultant film was annealed at 200 °C for 4 h to remove residual binders. EIS experiments were conducted under dark conditions with an applied potential, changing the frequencies in an electrolyte of 0.5 M NaSO<sub>4</sub>. The frequency range was from 1 mHz to 100 kHz under AC stimulus with a 5 mV amplitude. The impedance data of the equivalent circuit was recorded with ZMAN 2.2

software. A Mott-Schottky plot was exploited from the EIS measurement.

### **3.2.4 Photoluminescence spectroscopy**

Time-resolved photoluminescence (PL) measurements were conducted to observe decay spectra through time-correlated single photon counting methods using Fluo-Time 200 instrument (Picoquant, Germany). The 405 nm pulsed diode laser (pulse energy = 13 pJ, FWHM = 80 ps) with a repetition rate of 80 MHz was used as the excitation source. The signals were collected from the emissions of 1  $\mu$ M rhodamine B (RhB, Sigma). The extinction wavelength ( $\lambda_{em}$ ) was 580 nm. The fitting was evaluated by the reduced  $\chi^2$  value. The fluorescence signal was obtained through an automated motorized monochromator and then collected with a PicoHarp 300 unit. Data analyses were performed using a PicoQuant Fluofit software program.

### 3.2.5 Calculation of the interfacial area between Pt and TiO<sub>2</sub>



In order to quantify the extent, amount and rate of the charge separation of interface between Pt particles and TiO<sub>2</sub> support, interfacial areas between these two components are required, which were calculated based on the TEM images of Pt/TiO<sub>2</sub>. The shape of Pt NP was assumed to be spherical caps, and their sphere radii ( $r$ ) and heights ( $h$ ) were measured from TEM images and averaged.

Values for the volume of Pt NPs in Pt(x)/TiO<sub>2</sub>s were obtained from the radius and height by the following equation.

$$\text{Volume: } V = \int_{r-h}^r \pi(r^2 - z^2)dz = \pi r^2(r - (r - h)) - \frac{\pi}{3}(r^3 - (r - h)^3) = \pi h^2(r - \frac{h}{3})$$

Total number ratio of Pt NPs was calculated considering the ICP analysis results ( $w$ ) included in Table 3-1. Reciprocal of the obtained values for the volume is directly related to the total number ratio.

Ratio of the total number of Pt particles:  $\frac{w_1}{V_1} : \frac{w_2}{V_2} : \frac{w_3}{V_3}$

External surface area was obtained by integral of differential cylindrical surface along the z-axis.

$$x = \sqrt{r^2 - z^2}, \quad \frac{dx}{dz} = -\frac{z}{\sqrt{r^2 - z^2}} = -\frac{z}{x}, \quad dl = \sqrt{1 + \left(\frac{dx}{dz}\right)^2} dz = \frac{r}{x} dz,$$

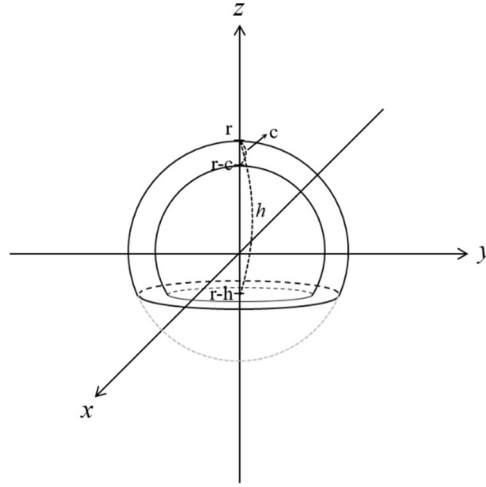
External surface area:  $S_{external} = 2\pi \int_{r-h}^r x dl = 2\pi rh$

Interfacial area was obtained by the area of a cut circle surface.

$$S_{interface} = \left(\sqrt{r^2 - (h-r)^2}\right)^2 \pi = 2\pi h\left(r - \frac{h}{2}\right)$$

Ratios of external surface area and interfacial area were obtained by multiplying the total number of Pt NPs and the averaged calculated areas. In order to verify this calculations, calculated external surface area ratio of Pt particle was compared to the experimentally measured external Pt surface area *via* CO chemisorption analysis (Table 3-2). The calculated ratio of the interfacial area between Pt and TiO<sub>2</sub> in Pt(1.7)/TiO<sub>2</sub>:Pt(3.3)/TiO<sub>2</sub>:Pt(5.1)/TiO<sub>2</sub> was 1.7:1.4:1 as that of the external Pt surface area was 3.51:1.88:1 (Table 3-2). The measured external surface areas of the Pt particle in the Pt(x)/TiO<sub>2</sub> systems were 3.91:2.17:1 as seen in Table 3-2, which is consistent with the calculated ratio. Thus, the calculated values were analogous to actual conditions, and the interfacial areas between Pt and TiO<sub>2</sub> were hardly changed by the Pt NP size variation.

### 3.2.6 Calculation of the external monolayer volume to total volume ratio of Pt NPs



The external monolayer volume ( $V_{\text{monolayer}}$ ) to total volume ratio of Pt NPs were obtained for the calculation of oxidized Pt amounts in Pt NPs when external monolayer of Pt NPs is assumed to be oxidized by the atmosphere. The symbol  $c$  indicates the Pt element diameter, which was 0.277 nm in the calculation.  $V_{\text{monolayer}}$  Was obtained by subtracting a small sphere cut of radius  $r-c$  from the original sphere cut.

$$V_{\text{monolayer}} = \int_{r-h}^r \pi(r^2 - z^2) dz - \int_{r-h}^{r-c} \pi((r-c)^2 - z^2) dz = \pi\left(\frac{2}{3}c^3 - rc^2 - hc^2 + 2rhc\right)$$

Finally, the ratios of expected oxidation amounts in Pt NPs were obtained by  $V_{\text{monolayer}}/V$ .

### 3.2.7 Finding the relationship between hole transfer and electron transfer between the Pt-TiO<sub>2</sub> interface under light irradiation conditions

In the semiconductor material following thermal equilibrium, the product of electron and hole concentration at constant temperature can be expressed by the following equation.

$$N_T \cdot P_T = N_c e^{-(E_c - E_F)/k_B T} \cdot N_v e^{-(E_F - E_v)/k_B T} = N_c N_v e^{-E_g/k_B T} = A \text{ (const.)}$$

In that equation,  $N_T$  is the electron carrier concentration,  $P_T$  is the hole carrier concentration,  $N_c$  is the effective density of states of the conduction band,  $N_v$  is the effective density of states of the valence band, and  $E_g$  is the band gap of the semiconductor material. Under light irradiation with energy,  $E > E_g$ , a quasi Fermi level should be considered, because the populations of electrons and holes are displaced from the thermal equilibrium. When a semiconductor is exposed to light, the electron or hole-carrier concentrations are maintained following equilibrium. Thus, the effect of the light source is diverted to the effect of the thermal source by introducing the quasi Fermi level and a quasi temperature to a Fermi-Dirac distribution function, which is expressed by the following equation [76-78].

$$f_0(E, E_F, T) = \frac{1}{1 + e^{(E - E_F)/k_B T}}$$

For the electrons in a conduction band, Fermi-Dirac distribution function considering Boltzmann approximation is expressed by the following equation.

$$f_c(k, r) \approx f_0(E, E_{F_c}, T_c) \approx e^{-(E - E_{F_c})/k_B T_c}$$

In that equation,  $E_{Fc}$  is the conduction band quasi Fermi level and  $T_c$  is the conduction band temperature. Holes in the valence band are expressed by the following equation.

$$f_v(k, r) \approx f_0(E, E_{Fv}, T_v) \approx 1 - e^{-(E_{Fv}-E)/k_B T_v}$$

In that equation,  $E_{Fv}$  is the valence band quasi Fermi level and  $T_v$  is the valence band temperature. Thus, electron and hole carrier concentration could be expressed according to the same logic used to derive thermal equilibrium case in semiconductors:

$$N_T = N_c e^{-(E_c - E_{Fc})/k_B T_c}, \quad P_T = N_v e^{-(E_{Fv} - E_v)/k_B T_v}$$

Therefore, product of electron and hole carrier concentrations could be expressed by the following equation.

$$\begin{aligned} N_T \cdot P_T &= N_c N_v e^{-(E_c - E_{Fc})/k_B T_c - (E_{Fv} - E_v)/k_B T_v} \leq N_c N_v e^{-(E_c - E_{Fc} + E_{Fv} - E_v)/k_B T_v} \\ &= N_c N_v e^{(-E_g + \Delta E_F)/k_B T_v} = B (const.) \end{aligned}$$

In the case of n-type semiconductors, the valence band temperature is greater than or equals to conduction band temperature. If two types of temperature are similar, the equation could be abbreviated to a simple form, which shows the diminishing effect of the bandgap,  $\Delta E_F$ , and increasing effect of temperature,  $(T_v - T)$ .

The  $TiO_2$  material used in our experiment was confirmed as n-type semiconductor according to its positive slope in a Mott-Schottky plot, and the above argument can be applied to our photocatalytic system under visible light. When the product of electron and carrier concentration is constant under

experimental conditions, the hole transfer rate constant from the TiO<sub>2</sub> valence band to Pt is the same magnitude but with an opposite sign to that of the electron transfer rate constant from the TiO<sub>2</sub> conduction band to Pt.

$$N_T \cdot P_T = N_c N_v e^{-(E_c - E_{Fc})/k_B T_c - (E_{Fv} - E_v)/k_B T_v} = C \text{ (const.)}$$

When hole concentration variation is considered, the following equation applies.

$$\frac{dP_T(t)}{dt} = -k_{T \rightarrow P}^+ P_T(t),$$

In that equation,  $-k_{T \rightarrow P}^+$  is hole transfer rate constant. The product conserved

between the two types of carrier concentrations, and  $P_T(t)$  can be expressed

as  $P_T(t) = \frac{C}{N_T(t)}$ . When the above hole carrier concentration variation

equation was substituted for the electron carrier concentration the following applied.

$$\frac{dP_T(t)}{dt} = C \cdot \frac{d}{dt} \left( \frac{1}{N_T(t)} \right) = C \cdot \frac{dN_T(t)}{dt} \cdot \frac{(-1)}{\{N_T(t)\}^2} = -k_{T \rightarrow P}^+ P_T(t) = -k_{T \rightarrow P}^+ \frac{C}{N_T(t)},$$

$$\frac{dN_T(t)}{dt} = k_{T \rightarrow P}^+ N_T(t),$$

$$\frac{dP_T(t)}{dt} = -k_{T \rightarrow P}^+ P_T(t) \leftrightarrow \frac{dN_T(t)}{dt} = k_{T \rightarrow P}^+ N_T(t)$$

Therefore, variations in the hole concentrations in the TiO<sub>2</sub> valence band varied in electron concentration in the TiO<sub>2</sub> conduction band in an opposite manner.

## 3.3 Results and discussion

### 3.3.1 Physicochemical properties of Pt/TiO<sub>2</sub>s

A shift in the Fermi level could become larger in inverse proportion to the size of the metal nanoparticles [79,80]. Thus, the Fermi level was carefully modulated by controlling the sizes of Pt nanoparticles to regulate the extent of charge transfer between Pt and TiO<sub>2</sub> materials. The 1 wt% Pt(x)/TiO<sub>2</sub>s, which have values for x = Pt NP diameter = 1.7, 3.3, and 5.1 nm, were carefully prepared by deposition-precipitation of Pt on commercial rutile-phase TiO<sub>2</sub> material with precise control of pH and temperature. The pH and the temperature were tailored in opposite directions to control the size of the Pt NPs. Electrostatic force was considered for the synthesis of desired size of Pt NPs. To obtain smaller Pt NPs, PtCl<sub>6</sub><sup>2-</sup> anions were dispersed to a negatively charged TiO<sub>2</sub> surface, which was obtained under higher pH conditions. Synthesis temperature should be decreased for higher pH conditions to avoid non-uniform growth on the TiO<sub>2</sub> surface and nucleation in the liquid phase. The pH was controlled to 5, 3, and 1 via NaOH or HNO<sub>3</sub> solutions, and temperatures were maintained at 10 °C, 50 °C, and 60 °C, respectively, for the preparation of Pt(1.7)/TiO<sub>2</sub>, Pt(3.3)/TiO<sub>2</sub>, and Pt(5.1)/TiO<sub>2</sub>. Then, thermal treatment was conducted under a hydrogen gas atmosphere to reduce the remaining oxide species of Pt. The ratios of the Pt element in the Pt/TiO<sub>2</sub>s were analyzed and determined to be approximately 1 wt% according to inductively coupled plasma (ICP) analysis results (Table 3-1). The size distributions of Pt nanoparticles in the Pt(x)/TiO<sub>2</sub>s were characterized by counting at least 150 particles according

to the transmission electron microscope (TEM) images, and distribution histograms were shown in Figure 3-1 and 3-2. The exposed Pt nanoparticle (NP) surfaces of Pt(x)/TiO<sub>2</sub>s were mainly composed of (111) and (100), according to Cs-corrected TEM (CS-TEM) images analyzed by fast Fourier transform (FFT) (Figure 3-1). The physicochemical properties of Pt/TiO<sub>2</sub>s were analyzed via ultraviolet-visible diffuse reflectance spectroscopy (UV-Vis DRS), X-ray diffraction spectroscopy (XRD), Brunauer-Emmett-Teller (BET), and CO adsorption, as shown in Figure 3-3, 3-4 and Table 3-2. The UV-Vis DRS spectra of TiO<sub>2</sub> and Pt(x)/TiO<sub>2</sub>s indicated that the bonding forms and interfacial areas between Pt and TiO<sub>2</sub> were similar (Figure 3-3). The bonding between Pt and TiO<sub>2</sub> in the Pt(x)/TiO<sub>2</sub> interfaces widened the main TiO<sub>2</sub> absorbance peak and increased the absorbance within the visible light region (>420 nm). The crystal phases of TiO<sub>2</sub> and Pt(x)/TiO<sub>2</sub>s were confirmed by XRD (Figure 3-4). Peaks corresponding to the rutile phase of TiO<sub>2</sub> were solely observed in all cases, and peak shifts of those were not observed, which indicated there was no atomic doping. Peaks from Pt nanoparticles were not observed due to the lower content and small size of Pt NPs. The BET surface areas of TiO<sub>2</sub> and Pt(x)/TiO<sub>2</sub>s were measured by N<sub>2</sub> adsorption-desorption analysis and identified to be maintained after the formation of Pt NPs on the TiO<sub>2</sub> support. In order to separate the M-S interfacial area effect from factors modulating the charge-separation amount and rate, the interfacial areas of Pt(x)-TiO<sub>2</sub>s were comparatively analyzed. The interface areas of Pt(x)/TiO<sub>2</sub>s were only minutely changed regardless of the Pt sizes according to CO chemisorption values and mathematical results (Table 3-2). Details of the process are included in the

supporting information. Thus, the energetic alignment of Pt-TiO<sub>2</sub> was mainly considered as the main factor in the following discussion.

For the detailed analysis for surface chemistry of the Pt/TiO<sub>2</sub> systems, the electronic states of elements in the Pt(x)/TiO<sub>2</sub>s were measured by X-ray photoelectron spectroscopy (XPS) (Figure 3-5 and 3-6). According to the deconvolution results of the Ti 2p XPS spectra (Figure 3-5a), there was negligible amounts of Ti<sup>3+</sup> in Pt/TiO<sub>2</sub>s which were less than 0.7% of total Ti species, and bare TiO<sub>2</sub> contained slightly more Ti<sup>3+</sup> than the Pt/TiO<sub>2</sub> systems, which was 1.9%. The O 1s XPS spectra also showed comparable OH<sup>-</sup> species amount among TiO<sub>2</sub> and Pt/TiO<sub>2</sub>s, except the existence of H<sub>2</sub>O residual in Pt(5.1)/TiO<sub>2</sub> and bare TiO<sub>2</sub>. Thus, it was confirmed that NaBH<sub>4</sub> or H<sub>2</sub> treatment in the Pt/TiO<sub>2</sub> synthesis process did not notably change the TiO<sub>2</sub> part. The Pt 4f XPS spectra showed that entire peaks were shifted to lower binding energies (BEs) relative to the generally known values of Pt species (Figure 3-6), due to the electron transfer from TiO<sub>2</sub> to Pt during Fermi level equilibration [81]. In the Fermi-level alignment process, a larger difference between the Fermi level of Pt and TiO<sub>2</sub> required a greater level of electron transfer from TiO<sub>2</sub> to Pt until equilibrium could be reached, which corresponded to a Pt/TiO<sub>2</sub> system with smaller Pt NPs. However, the smaller the Pt nanoparticles, the more likely it was that those Pt elements would exist in states of losing electrons and increased oxidation. Thus, an origin of oxidized Pt species was discussed to bridge a gap between the theoretical expectation and the experimental observation. The oxidized Pt species should come from an external Pt NP surface contacting the atmosphere, since a strong reducing condition was

maintained in the synthesis of Pt NPs on TiO<sub>2</sub> support, and Pt cannot be existed in states of oxidation between the Pt-TiO<sub>2</sub> interface. The smaller Pt nanoparticles in Pt/TiO<sub>2</sub> had a higher external surface-to-volume ratio and consisted of surface atoms with a lower coordination number that allows easy oxidation. Consequently, it is enough to compare the amounts of oxidized Pt species from observation with those from calculation assuming fully oxidized Pt external monolayer, for an elucidation of the electron transfer from TiO<sub>2</sub> to Pt under the Fermi level alignment. The ratios of (Pt<sup>4+</sup>+ Pt<sup>2+</sup>)/Pt<sub>total</sub> were 0.38, 0.32, and 0.24 for Pt(1.7), Pt(3.3) and Pt(5.1)/TiO<sub>2</sub> according to the Pt 4f XPS spectra, and 0.56, 0.31, and 0.17 from the calculation. Therefore, smaller Pt NPs in the Pt(x)/TiO<sub>2</sub> system obviously received a greater number of electrons from TiO<sub>2</sub>, based on the difference between the expected oxidized ratio of Pt(x)/TiO<sub>2</sub> and that from XPS measurement, which supports a larger difference of the Fermi levels between the smaller Pt and TiO<sub>2</sub>.

### **3.3.2 Band alignment modulations of Pt/TiO<sub>2</sub> systems**

The lower Fermi level of smaller Pt could increase band bending extent in TiO<sub>2</sub>, which supports an enhanced total charge separation process (Figure 3-7). The sharper slope of the TiO<sub>2</sub> VB portion between the Pt-TiO<sub>2</sub> interfaces could induce faster movement of hole carriers due to the higher internal electric field. The slope on TiO<sub>2</sub> CB could block the weakly excited electron transfer from the TiO<sub>2</sub> CB to Pt and allowed a faster hot electron transfer from Pt to the TiO<sub>2</sub> CB at the same time. Thus, flat-band potentials for TiO<sub>2</sub> and Pt(x)/TiO<sub>2</sub>s were

obtained from the Mott-Schottky plot (Figure 3-8a) for the observation of band bending variation among Pt(x)/TiO<sub>2</sub>s (Figure 3-8b). Experimental variables except the Pt size were identically fixed. The Fermi level of Pt and reported Energy levels of TiO<sub>2</sub> CB and VB [66,82-85] are considered for comparative analysis. The Pt(x)/TiO<sub>2</sub>-electrolyte interface of  $C_{SC}^{-2}$  and the carrier density of  $N_D$  are given in equations (1) [86,87].

$$\frac{1}{C_{SC}^2} = \left( \frac{2}{e\epsilon\epsilon_0 N_D} \right) \left[ (V - V_{fb}) - \frac{k_B T}{e} \right] \quad (1)$$

In the equation (1),  $V$  is the applied potential,  $V_{fb}$  is the flat-band potential,  $e$  is the elementary charge,  $\epsilon_0$  is vacuum permittivity, and  $\epsilon$  is the dielectric constant of the electrode material. The flat-band potential can be obtained from the x-intercept via the equation (1). When the flat-band potentials ( $V_{fb}$ ) of Pt(x)/TiO<sub>2</sub>s were compared with bare TiO<sub>2</sub>, those were gradually negatively shifted with decrement of Pt NP size. The Mott-Schottky plot is originated from a flat electrode model and may contain errors in determining the band bending extent of the Pt-TiO<sub>2</sub> nanostructure. However, supported 1 wt% Pt component would not significantly change the structure of Pt(x)/TiO<sub>2</sub>s compared to bare TiO<sub>2</sub>. The shift of flat band potential could be from band bending between the Pt-TiO<sub>2</sub> interface [88,89]. Band bending was confirmed to be increased in the Pt/TiO<sub>2</sub> system containing small Pt NPs, which is in accordance with the theoretical expectation for Fermi level variation of Pt (Figure 3-8b). When the Pt/rutile TiO<sub>2</sub> system is activated by visible light, charge separation between Pt-TiO<sub>2</sub> interface could be modulated depending on the band bending degree. Therefore, charge separation amount and rate were observed and correlated to

band bending variation in Pt(x)/TiO<sub>2</sub>s in the following discussion.

### **3.3.3 Observations of charge separation between Pt-TiO<sub>2</sub> interfaces under visible light**

The extent of charge separation between Pt and TiO<sub>2</sub> was identified from the XANES spectra (Figure 3-7). White line intensities were changed after visible light (>400 nm) irradiation. Due to the 3 eV band gap of the rutile phase TiO<sub>2</sub>, electrons in the VB can absorb a portion of the visible light and were excited to the CB, according to the UV-Vis DRS spectra (Figure 3-3). Therefore, under visible light irradiation, if excited electrons in the CB have energy sufficient to overcome the Schottky barrier, the intensity of the Pt white lines should be decreased in accordance with many charge-transfer mechanisms, as reported in recent studies [90,91]. However, the intensity of the white lines was increased in all Pt(x)/TiO<sub>2</sub> cases, which means that the electrons in the Pt nanoparticles were transferred to TiO<sub>2</sub>. Pt(x)/TiO<sub>2</sub> containing smaller Pt shows larger differences in white line intensity under light on/off conditions. Smaller Pt NPs on Pt(x)/TiO<sub>2</sub> become more positively charged by the charge separation process under a state of dynamic equilibrium. The tendency of band bending increment (Figure 3-8a) is similar to increase in the white line intensities after visible light irradiation (Figure 3-7), which empowers the charge separation mechanism by composited electrons and hole transport under visible light. To identify both the charge-transfer path and rate in the Pt/TiO<sub>2</sub> system, kinetic analysis was conducted.

### 3.3.4 Kinetic analysis of charge separation between Pt-TiO<sub>2</sub> interfaces

Kinetic charge-transport processes in the Pt/TiO<sub>2</sub> systems were identified in detail by fitting the time-resolved photoluminescence (PL) spectra of TiO<sub>2</sub> and Pt(x)/TiO<sub>2</sub>s (Figure 3-9a) [60,61,92]. In the measurement of time-resolved PL, two types of PL from Rhodamine B (RhB) dye and TiO<sub>2</sub> were generated under the experimental conditions. Excited electrons from RhB are transferred to either a TiO<sub>2</sub> or a Pt/TiO<sub>2</sub> system, which forms an electron transfer path in a photocatalytic system. An electron transfer rate constant from Pt to TiO<sub>2</sub> and a hole transfer rate constant from TiO<sub>2</sub> to Pt were obtained from the overall electron-transfer path. The charge-transfer path is generally considered from the aspect of electrons under our time-resolved PL experimental conditions (Figure 3-10), and the hole transfer from the TiO<sub>2</sub> VB to Pt seemed contradictive from an intuitive aspect. However, due to the fact that the products of electron and hole carrier concentration were conserved under the same temperature and constant light irradiation conditions, it was mathematically confirmed that the absolute values of the hole transfer rate constant from TiO<sub>2</sub> VB and the electron transfer rate constant from TiO<sub>2</sub> CB were the same, but with opposite signs (Figure 3-11). Figure 3-9b shows the two operating types of charge-transfer processes under visible light irradiation conditions. Under the photocatalytic conditions of Pt/TiO<sub>2</sub>, electron-hole charge separation occurred via visible light excitation of both Pt and rutile TiO<sub>2</sub>. Rutile TiO<sub>2</sub> could be excited by visible light and only holes in the TiO<sub>2</sub> VB

could transfer to Pt. Excited electron could be formed on Pt NPs and directly transferred to the TiO<sub>2</sub> CB. There was a net electron transfer between the Pt-TiO<sub>2</sub> interface from Pt to the TiO<sub>2</sub> CB in both cases. The time-resolved spectra of TiO<sub>2</sub> and Pt(x)/TiO<sub>2</sub>s is expressed by the sum of two exponential decay functions, as shown in equation (2).

$$I(t) = \sum_{i=1}^2 A_i e^{-\frac{t}{\tau_i}} \quad (2)$$

In equation (2),  $\tau_i$  is the decay time and  $A_i$  represents the amplitude of the PL from components at  $t=0$ . One exponential function represents the emission of RhB and the other represents that of TiO<sub>2</sub>. Kinetic parameters representing the two PLs are included in the supporting information (Table 3-3). The overall charge-transfer path and derivation procedure for the charge-transfer rate constants are described in Figure 3-9b, 3-10 and Table 3-4. Calculation of the electron transfer rate from Pt to the TiO<sub>2</sub> CB was based on the PL of RhB. The overall charge-transfer rate constants were calculated and are included in Table 3-5. The electron-transfer rate ( $k_{R \rightarrow P \rightarrow T}$ ) from Pt and the hole-transfer rate ( $k_{T \rightarrow P}^+$ ) from TiO<sub>2</sub> both were rapidly increased when the size of the Pt NPs in Pt(x)/TiO<sub>2</sub> were decreased (Figure 3-12). The larger band bending could be a main factor, since a higher electric field is formed between the Pt-TiO<sub>2</sub> interface. The increments of two respective charge separation rates were different.  $k_{T \rightarrow P}^+$  is much higher than  $k_{R \rightarrow P \rightarrow T}$  in case of Pt(5.1)/TiO<sub>2</sub>, which suggests that hole transfer process would be more dominant process than hot electron transfer process in a photocatalytic condition.  $k_{R \rightarrow P \rightarrow T}$  was more drastically increased than  $k_{T \rightarrow P}^+$  depending on Pt size, and a contribution of the two charge

separation rates were comparable in the Pt(1.7)/TiO<sub>2</sub> system. Above results could be come from the opposite curvature of band bending of TiO<sub>2</sub> CB and VB in the aspect of different charge carriers (Figure 3-12). A hot electron transfer path on TiO<sub>2</sub> CB is concave and a hole transfer path on TiO<sub>2</sub> VB is convex. Thus, movement of electrons would be increasingly effective than holes when band is more bended.

### 3.3.5 Photocatalytic activity test

The acetaldehyde photocatalytic reaction was investigated in the gas phase to evaluate the influence of charge separation on Pt(x)/TiO<sub>2</sub>s under visible light ( $\lambda > 400$  nm), as shown in Figure 3-12 and 3-13. Performances under visible light on/off conditions were included in Figure 3-13, and acetaldehyde was negligibly decreased in the dark condition. Rutile TiO<sub>2</sub> and Pt NP were simultaneously excited by visible light and as a consequence electrons accumulated on the TiO<sub>2</sub> CB and holes in the Pt NP. Electrons on TiO<sub>2</sub> CB converted oxygen to superoxide anions, which sequentially degraded the acetaldehyde (Figure 3-14). A role of holes in Pt NPs have not been completely revealed, and holes might act as acetaldehyde adsorption site [69] or dissociation agent of Ti-O bond existed in partially oxidized acetaldehyde species [93]. Pt(x)/TiO<sub>2</sub>s showed better performance than bare TiO<sub>2</sub>, as a result of the interfacial charge separation at the Pt(x)/TiO<sub>2</sub> interfaces. As shown in Figure 3-12, the decreasing rates for acetaldehydes were 0.359, 0.239, and 0.197 h<sup>-1</sup> for Pt(1.7), Pt(3.3), and Pt(5.1)/TiO<sub>2</sub> respectively, assuming first-

order kinetics. This means that the activities of Pt(x)/TiO<sub>2</sub>s were gradually increased in the system containing small Pt NPs, which induced a fast and large amount of charge separation. The electron transfer rate constants ( $k_{R \rightarrow P \rightarrow T}$ ), the hole transfer rate constants ( $k_{T^+ \rightarrow P}$ ), and the acetaldehyde photo-oxidation rates are concurrently listed. A larger amount of hole generation on Pt NPs conserves excited charge carriers from recombination, which in turn ensures faster oxidation of the reactant. When the electron transfer from Pt to the TiO<sub>2</sub> CB and the hole transfer from the TiO<sub>2</sub> VB to Pt were increased, acetaldehyde conversion rates were also similarly increased, as anticipated.

**Table 3-1.** Measurement of the Pt element concentration in Pt(x)/TiO<sub>2</sub> systems according to ICP analysis.

Entry	Pt amount (wt %)
Pt(1.7)/TiO <sub>2</sub>	0.97
Pt(3.3)/TiO <sub>2</sub>	1.02
Pt(5.1)/TiO <sub>2</sub>	1.06

**Table 3-2.** Calculated external surface area of Pt(x) and the interfacial area of Pt(x)/TiO<sub>2</sub>. Experimentally measured surface area of Pt(x)/TiO<sub>2</sub> and Pt(x) based on BET and CO adsorption analysis.

Entry	Surface area of Pt(x) by CO adsorption (m <sup>2</sup> /g-metal)	Calculated external surface area of Pt(x) (m <sup>2</sup> /g-catal)	Calculated interface surface area of Pt(x)/TiO <sub>2</sub> (m <sup>2</sup> /g-catal)	Surface area of Pt(x)/TiO <sub>2</sub> by BET (m <sup>2</sup> /g-catal)
TiO <sub>2</sub>	-	-	-	38.9
Pt(1.7)/TiO <sub>2</sub>	21.5	1.12	0.17	40.0
Pt(3.3)/TiO <sub>2</sub>	12.0	0.60	0.14	36.4
Pt(5.1)/TiO <sub>2</sub>	5.5	0.32	0.10	35.6

**Table 3-3.** Kinetic parameters extracted from fitted results of the time-resolved PL spectra. The first PL is from Rhodamine B, and the second is from TiO<sub>2</sub>.

Entry	A <sub>1</sub>	$\tau_1$ (ns)	A <sub>2</sub>	$\tau_2$ (ns)	$\chi^2$
Rhodamine B	12213	1.44			0.985
TiO <sub>2</sub>	10226	1.41	80.7	3.03	0.969
Pt(1.7)/TiO <sub>2</sub>	10317	1.31	77.3	3.91	0.985
Pt(3.3)/TiO <sub>2</sub>	10618	1.38	61.5	3.52	0.972
Pt(5.1)/TiO <sub>2</sub>	11809	1.40	59.6	3.41	0.982

**Table 3-4.** Calculating processes of governing equations for charge transfer rate constants, and electron transfer rate constants in RhB, TiO<sub>2</sub> in RhB, and Pt(x)/TiO<sub>2</sub> in RhB. The hole-transfer rate constants were particularly important to consider in the Pt(x)/TiO<sub>2</sub>s.

System	Governing equation and solution for Charge transfer rate constants	Calculated rate constants
RhB solution	(i) $\frac{dN_R}{dt} = -k_R N_R$ $\rightarrow N_R = N_{R0} e^{-k_R t}$	$k_R = \frac{1}{\tau_{1,RhB}}$
TiO <sub>2</sub> +	(i) $\frac{dN_R}{dt} = -(k_R + k_{R \rightarrow T}) N_R$ $\rightarrow N_R = N_{R0} e^{-(k_R + k_{R \rightarrow T}) t}$	$k_{R \rightarrow T} = \frac{1}{\tau_{2,TiO_2}} + \frac{1}{\tau_{1,RhB}}$
RhB solution	(ii) $\frac{dN_T}{dt} = k_{R \rightarrow T} N_R - k_T N_T$ $\rightarrow N_T = C_1 e^{-(k_R + k_{R \rightarrow T}) t} + C_2 e^{-k_T t}$	$k_T = \frac{1}{\tau_{2,TiO_2}}$
Pt(x)/TiO <sub>2</sub> +	(i) $\frac{dN_R}{dt} = -(k_R + k_{R \rightarrow T} + k_{R \rightarrow P \rightarrow T}) N_R$ $\rightarrow N_R = N_{R0} e^{-(k_R + k_{R \rightarrow T} + k_{R \rightarrow P \rightarrow T}) t}$	$k_{R \rightarrow P \rightarrow T} = \frac{1}{\tau_{1,Pt(x)/TiO_2}} + \frac{1}{\tau_{1,TiO_2}}$
TiO <sub>2</sub> +	(ii) $\frac{dN_T}{dt} = k_{R \rightarrow T} N_R - (k_T - (-k_{T \rightarrow P})) N_T$ $= k_{R \rightarrow T} N_R - (k_T - k_{T \rightarrow P}^+) N_T$	$k_{T \rightarrow P}^+ = -k_{T \rightarrow P}$
RhB solution	$\rightarrow N_T = C_3 e^{-(k_R + k_{R \rightarrow T} + k_{R \rightarrow P \rightarrow T}) t} + C_4 e^{-(k_T - (-k_{T \rightarrow P})) t}$ $= C_3 e^{-(k_R + k_{R \rightarrow T} + k_{R \rightarrow P \rightarrow T}) t} + C_4 e^{-(k_T - k_{T \rightarrow P}^+) t}$	$= -\frac{1}{\tau_{2,Pt(x)/TiO_2}} + \frac{1}{\tau_{2,TiO_2}}$
$C_1 = \frac{k_{R \rightarrow T}}{k_T - (k_R + k_{R \rightarrow T})} \cdot N_{R0}$		$C_3 = \frac{k_{R \rightarrow T}}{(k_T + k_{T \rightarrow P}) - (k_R + k_{R \rightarrow T} + k_{R \rightarrow P \rightarrow T})} \cdot N_{R0}$
$C_2 = N_{T0} - C_1$		$C_4 = N_{T0} - C_3$

**Table 3-5.** Charge-transfer rate constants of TiO<sub>2</sub> and Pt(x)/TiO<sub>2</sub> systems derived from the fitted results of the time-resolved PL spectra, according to processes used for calculation (Table 3-4).

Entry	$k_R$ (10 <sup>8</sup> s <sup>-1</sup> )	$k_T$ (10 <sup>8</sup> s <sup>-1</sup> )	$k_{R \rightarrow P \rightarrow T}$ (10 <sup>8</sup> s <sup>-1</sup> )	$k_{T \rightarrow P}^+$ (10 <sup>8</sup> s <sup>-1</sup> )
TiO <sub>2</sub>			-	-
Pt(1.7)/TiO <sub>2</sub>	0.69473	0.33058	0.05328	0.07469
Pt(3.3)/TiO <sub>2</sub>			0.01818	0.04655
Pt(5.1)/TiO <sub>2</sub>			0.00828	0.03732

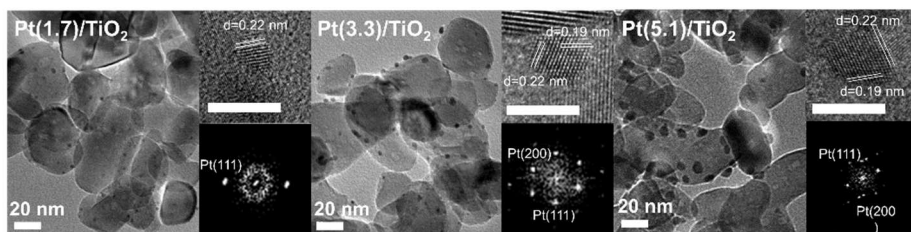


**Figure 3-1.** TEM and Cs-TEM images of Pt(1.7)/TiO<sub>2</sub>, Pt(3.3)/TiO<sub>2</sub>, and Pt(5.1)/TiO<sub>2</sub>. Each x value in Pt(x)/TiO<sub>2</sub> systems means an averaged Pt nanoparticle size. Scale bars in Cs-TEM images indicate 1 nm. FFT patterns were obtained from a Pt NP in the Cs-TEM images.

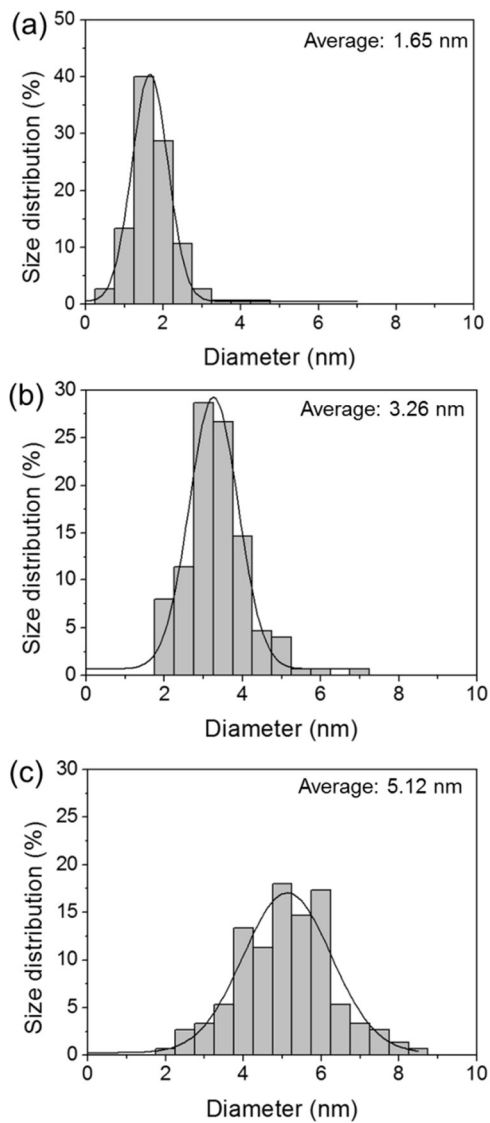


**Figure 3-2.** Pt NP size distributions in (a) Pt(1.7)/TiO<sub>2</sub>, (b) Pt(3.3)/TiO<sub>2</sub>, and (c) Pt(5.1)/TiO<sub>2</sub>.

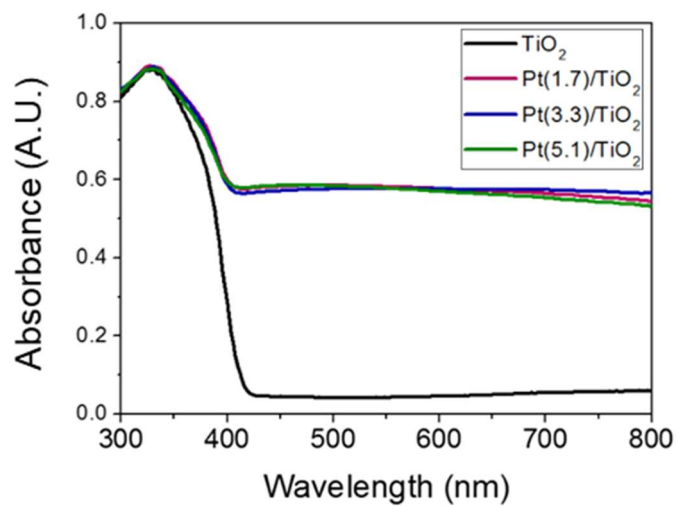


**Figure 3-3.** UV-Vis DRS spectra of  $\text{Pt}(x)/\text{TiO}_2$  systems.

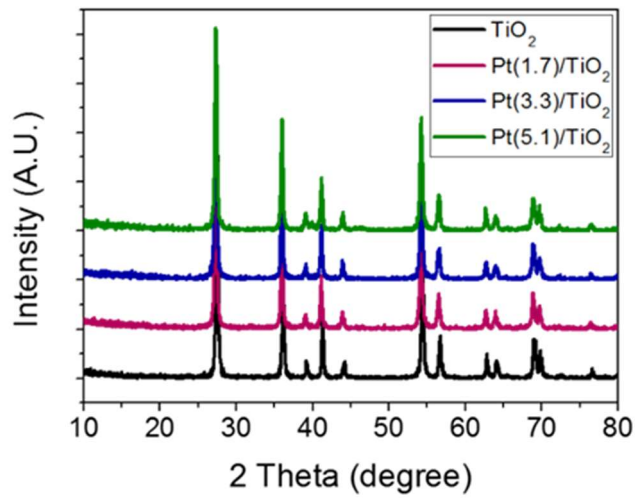


**Figure 3-4.** X-ray diffraction spectra of  $\text{Pt}(x)/\text{TiO}_2$  systems.

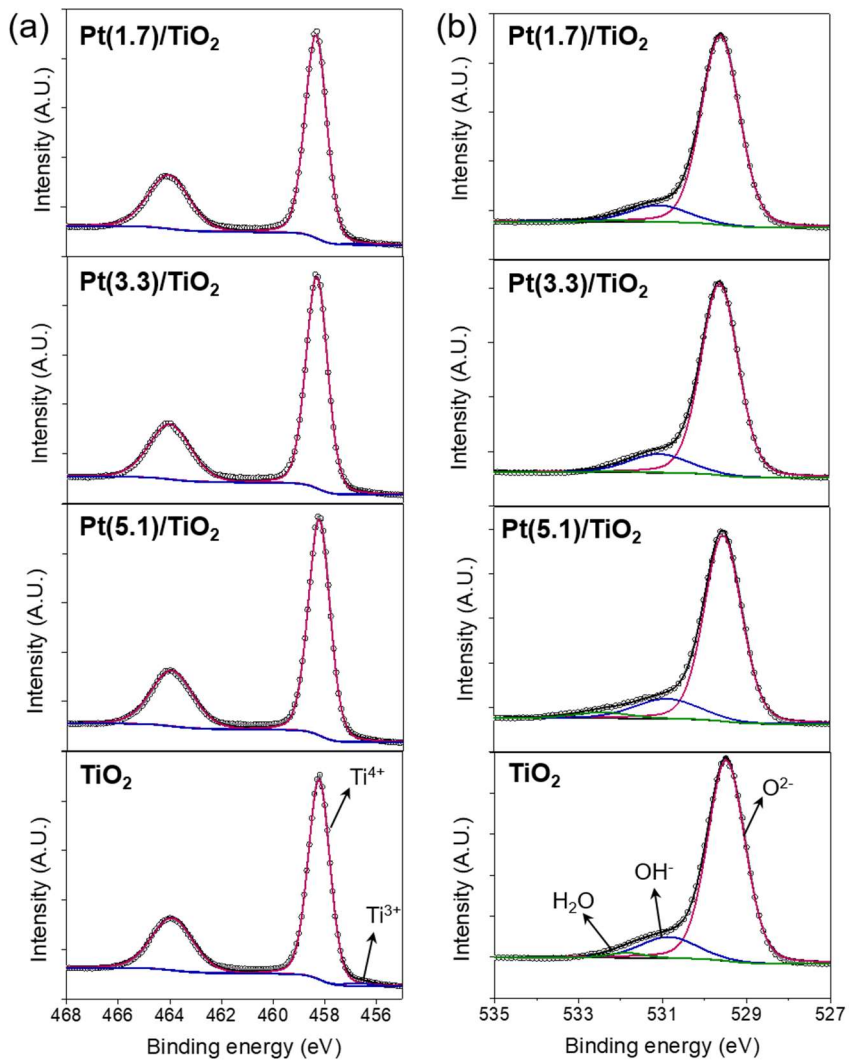


**Figure 3-5.** (a) Ti 2p and (b) O 1s XPS spectra of Pt(1.7)/TiO<sub>2</sub>, Pt(3.3)/TiO<sub>2</sub>, Pt(5.1)/TiO<sub>2</sub> and TiO<sub>2</sub>.

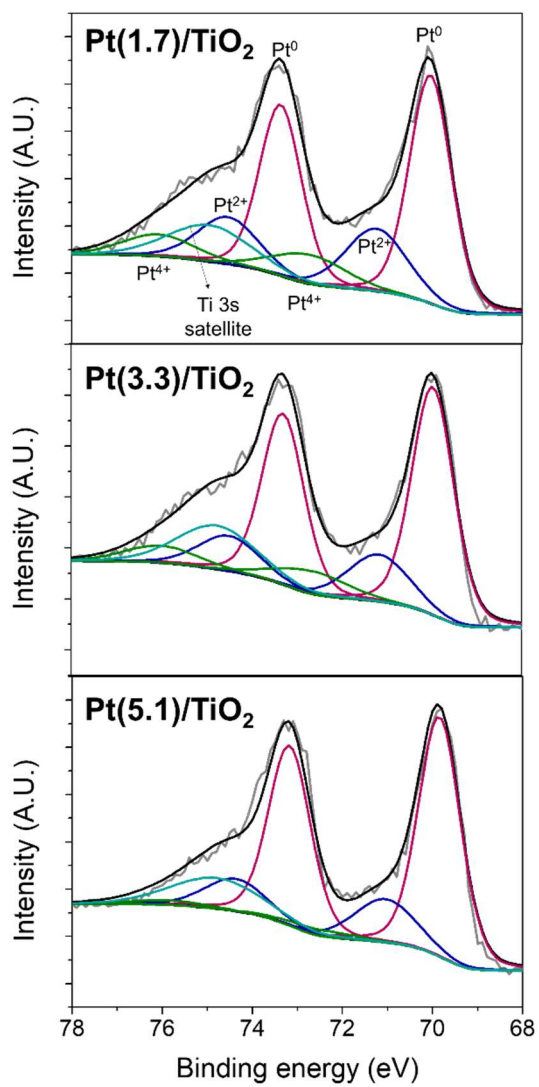


**Figure 3-6.** Pt 4f XPS spectra of Pt(1.7)/TiO<sub>2</sub>, Pt(3.3)/TiO<sub>2</sub>, Pt(5.1)/TiO<sub>2</sub> and TiO<sub>2</sub>.

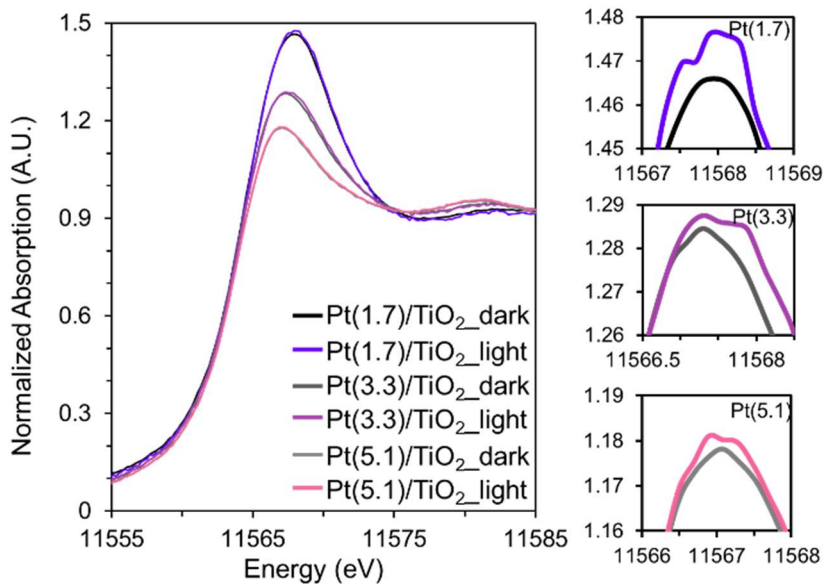


**Figure 3-7.** Pt L3 edge XANES spectra of Pt(x)/ TiO<sub>2</sub>s before and after visible light irradiation condition. The enlarged ranges show the white line differences.

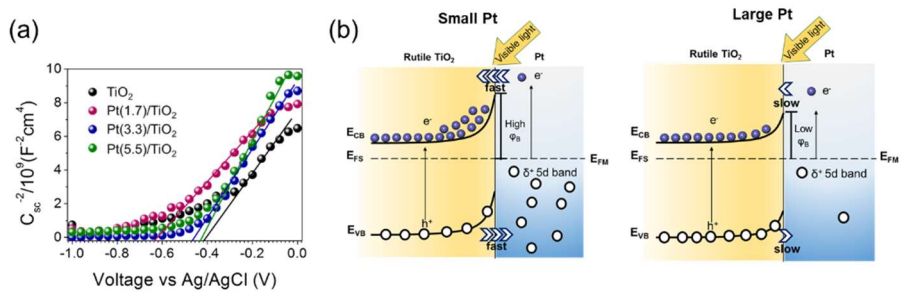


**Figure 3-8.** (a) Mott–Schottky plot of  $\text{TiO}_2$  and  $\text{Pt}(x)/\text{TiO}_2$  systems for the observation of flat band potential under dark condition. (b) Schematic energy diagrams of  $\text{Pt}/\text{TiO}_2$  systems with Pt NP size variation when visible light is irradiated.

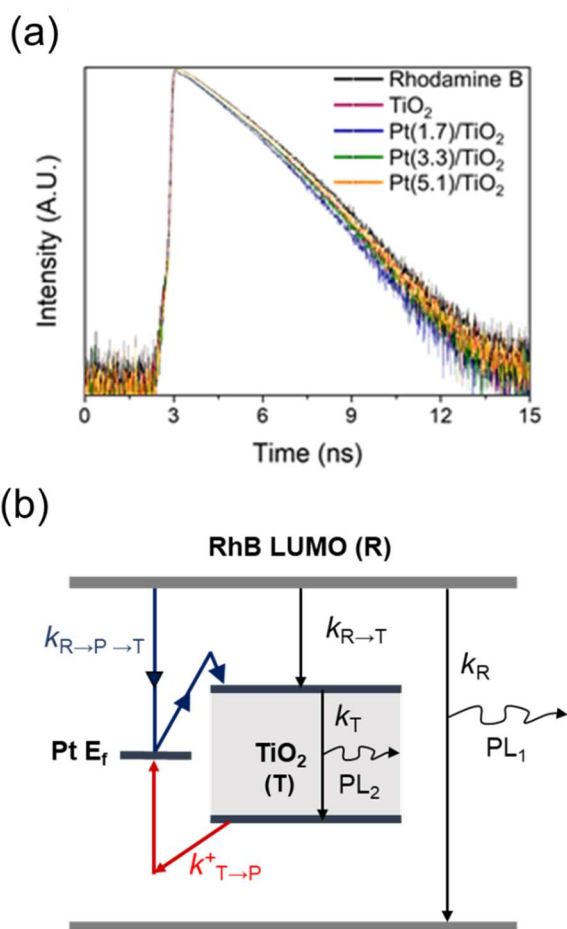


**Figure 3-9.** (a) Time-resolved photoluminescence spectra (PL) of  $\text{TiO}_2$  and  $\text{Pt}(x)/\text{TiO}_2$  systems in the RhB solutions with 580 nm emission where laser excitation was 405 nm. (b) Charge transfer path of  $\text{Pt}/\text{TiO}_2$  in the time-resolved PL measurement condition. Electron transfer rate constants were denoted as black and blue arrows, and a hole transfer rate as red arrows.

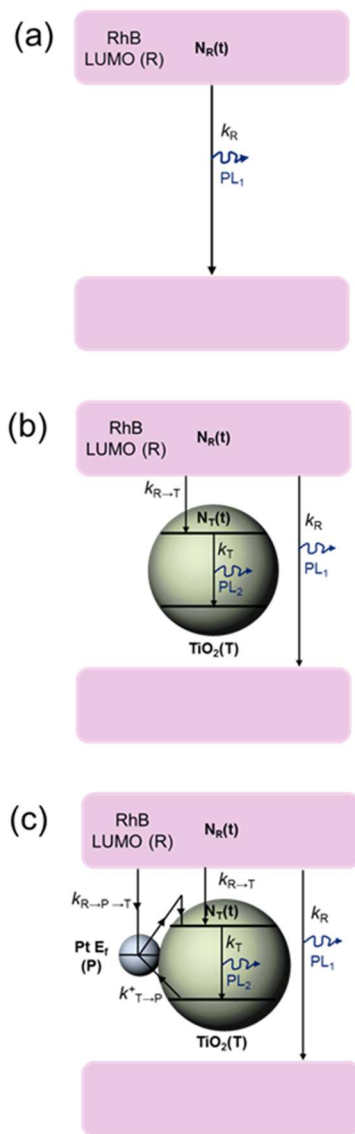


**Figure 3-10.** Electron transfer paths under conditions of (a) a RhB solution, (b)  $TiO_2$  in the RhB solution, and (c) Pt(x)/ $TiO_2$  in the RhB solution with a laser excitation wavelength of 405 nm and an emission wavelength of 580 nm.

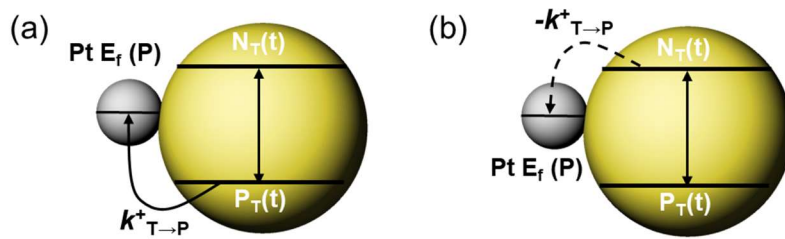


**Figure 3-11.** Two congruent pictures at the point of kinetics. When a product of electron and hole carrier concentration remains constant, (a) the hole transfer from the TiO<sub>2</sub> VB to Pt ( $k_{T→P}^+$ ) can be treated as (b) an electron transfer from Pt to the TiO<sub>2</sub> CB ( $-k_{T→P}^+$ ) according to the mathematical consequence.

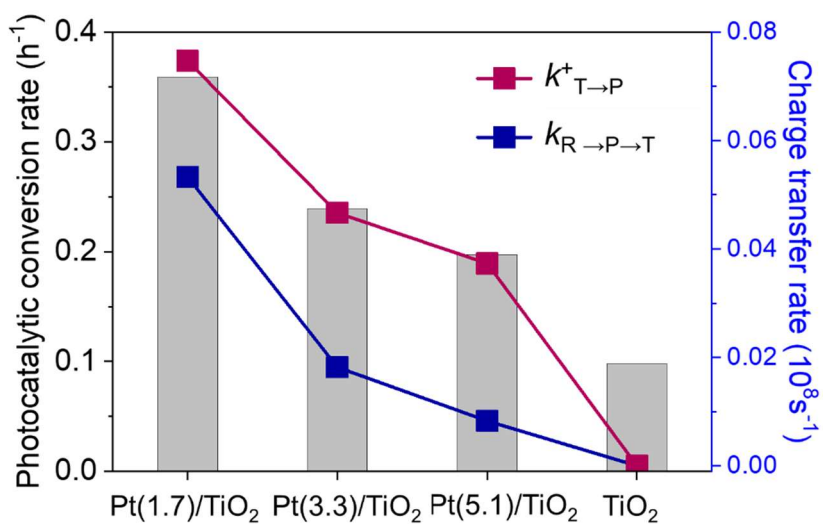


**Figure 3-12.** Comparison of acetaldehyde conversion rates and charge separation rate constants. The acetaldehyde oxidation rate, which is related to hole consumption, was indicated by gray bar. The hole transfer rate ( $k_{T \rightarrow P}^+$ ) was expressed by red line and the electron transfer rate ( $k_{R \rightarrow P \rightarrow T}$ ) by blue line.

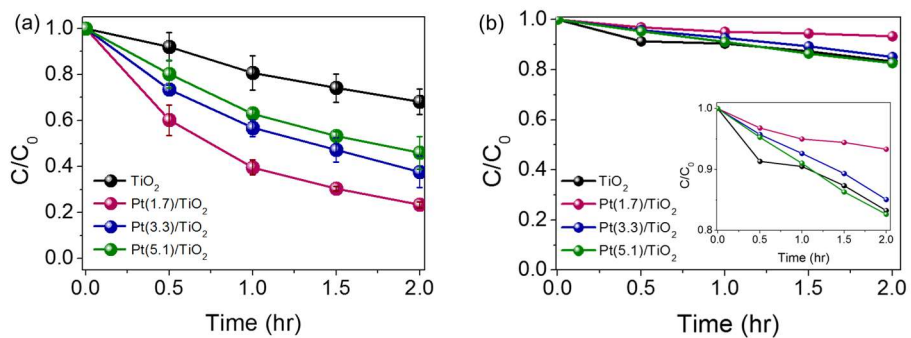


**Figure 3-13.** Photocatalytic rate of Pt(x)/TiO<sub>2</sub> in acetaldehyde oxidation under (a) visible light irradiation (>400 nm) and (b) dark conditions with an enlarged inset.

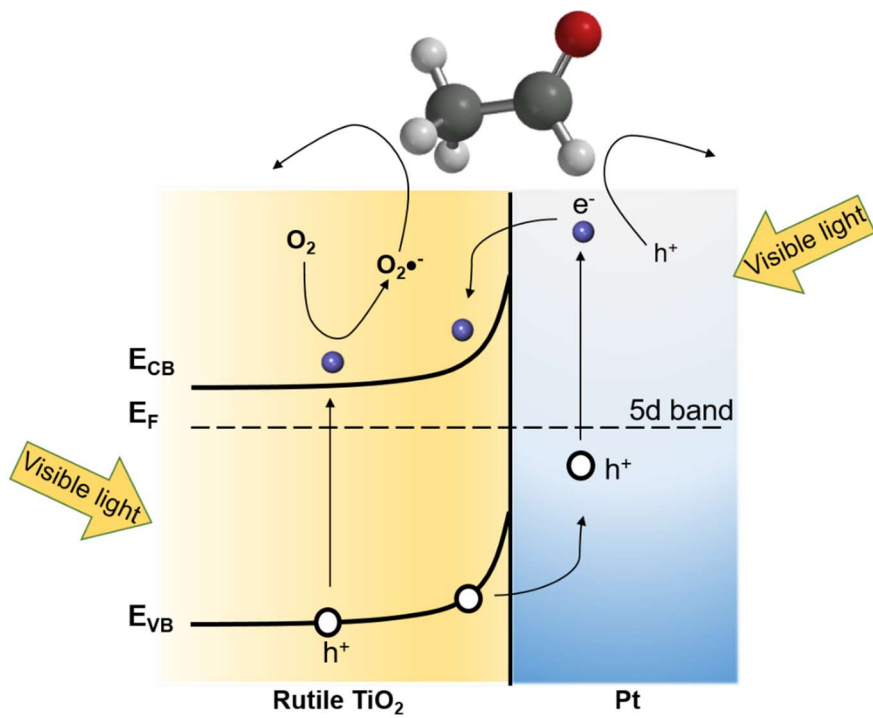


**Figure 3-14.** Schematic mechanism for acetaldehyde photodegradation by hole consumption, which could be generated by the hole transport from  $\text{TiO}_2$  and the hot electron generation from Pt.

## Chapter 4. Summary and Conclusions

Au supported on 3D hierarchical rutile TiO<sub>2</sub> was verified as an optimized plasmonic photocatalyst under conditions of visible light by considering crystal phase and morphology, which are considered to be two basic factors. It was able to observe a prolonged LSPR lifetime and enhanced Au plasmonic interaction in 3D morphology by a confined structure effect. In the light of photocatalytic activity, which is deeply related to the rate of generation of hydroxyl radicals, the hot electron transfer rate from Au to TiO<sub>2</sub> ( $k_{R \rightarrow A \rightarrow T}$ ) appears to be the main determinant. When  $k_{R \rightarrow A \rightarrow T}$  was compared under conditions of the same morphology and a different crystal phase of Au/TiO<sub>2</sub>, Au/rutile TiO<sub>2</sub> showed a 2.9 times higher value than Au/anatase TiO<sub>2</sub>. The findings revealed that due to the stronger bond between Au and rutile TiO<sub>2</sub> and the overlapping of Au DOS in the rutile TiO<sub>2</sub> CB, Au/rutile TiO<sub>2</sub> is more advantageous in both hot electron transfer and the quantity of electrons. Furthermore, the reverse transfer path is obstructed in Au/rutile TiO<sub>2</sub>, due to the larger band bending induced by thermodynamic energy level of rutile TiO<sub>2</sub> CB, which delays the recombination between electrons and holes in Au.

An effective charge-separation pathway was proposed in the M-S junctioned photocatalytic system via a synergetic electron and hole-transfer mechanism in

visible light regions when the transfer of excited electrons from a semiconductor CB to metal is improbable (Figure 3-2b). To modulate the extent of electron and hole transfer from energetic and kinetic aspects, A Pt/TiO<sub>2</sub> system was adopted with adjustable Fermi levels via control of the sizes of supported Pt NPs. Lowering the Fermi level of Pt in the Pt/TiO<sub>2</sub> system creates larger electric fields in both the TiO<sub>2</sub> VB and CB, which increases the amount of hole transfer from the TiO<sub>2</sub> VB to Pt and electron transfer from Pt to the TiO<sub>2</sub> CB. The amount and rate of composite electron and hole transfer were directly related to the photocatalytic performance in the hole-mediated acetaldehyde photo-oxidation reaction. I expect this study will contribute to the rational design of multicomponent photocatalytic systems from the aspect of energetic alignment.

## Bibliography

- [1] T. Hirakawa, P. V. Kamat, *J. Am. Chem. Soc.* **2005**, 127, 3928-3934.
- [2] J. Yu, G. Dai, B. Huang, *J. Phys. Chem. C* **2009**, 113, 16394-16401.
- [3] Z. Liu, W. Hou, P. Pavaskar, M. Ayko, *Nano Lett.* **2011**, 11, 1111-1116.
- [4] N. Chandrasekharan, P. V. Kamat, *J. Phys. Chem. B* **2000**, 104, 10851-10857.
- [5] Y. Tian, T. Tatsuma, *J. Am. Chem. Soc.* **2005**, 127, 7632-7637.
- [6] C. G. Silva, R. Juárez, T. Marino, R. Molinari, H. García, *J. Am. Chem. Soc.* **2011**, 133, 595-602.
- [7] G. Zhou, X. Xu, T. Ding, B. Feng, Z. Bao, J. Hu, *ACS Appl. Mater. Interfaces* **2015**, 7, 26819-26827.
- [8] F.-X. Xiao, Z. Zeng, S.-H. Hsu, S.-F. Hung, H. M. Chen, B. Liu, *ACS Appl. Mater. Interfaces* **2015**, 7, 28105-28109.
- [9] C. Yu, W. Zhou, L. Zhu, G. Li, K. Yang, R. Jin, *Appl. Catal. B* **2016**, 184, 1-11.
- [10] C. Yu, G. Li, S. Kumar, H. Kawasaki, R. Jin, *J. Phys. Chem. Lett.* **2013**, 4, 2847-2852.
- [11] S. Bouhadoun, C. Guillard, F. Dapozze, S. Singh, D. Amans, J. Bouclé, N. Herlin-Boime, *Appl. Catal. B* **2015**, 174-175, 367-375.
- [12] M. Tahir, B. Tahir, N. A. S. Amin, *Appl. Surf. Sci.* **2015**, 356, 1289-1299.
- [13] L. G. Devi, R. Kavitha, *Appl. Surf. Sci.* **2016**, 360, 601-622

- [14] X. Wang, R. Yu, K. Wang, G. Yang, H. Yu, *Chin. J. Catal.* **2015**, 36, 2211-2218.
- [15] J. Jiang, J. Yu, S. Cao, *J. Colloid Interface Sci.* **2016**, 461, 56-63.
- [16] S. Das, S. Sinha, M. Suar, S.-I. Yun, A. Mishra, S. K. Tripathy, *J. Photochem. Photobiol. B* **2015**, 142, 68-76.
- [17] D. Jiang, W. Wang, S. Sun, L. Zhang, Y. Zheng, *ACS Catal.* **2015**, 5, 613-621.
- [18] F. Meng, S. K. Cushing, J. Li, S. Hao, N. Wu, *ACS Catal.* **2015**, 5, 1949-1955.
- [19] L. Wu, F. Li, Y. Xu, J. W. Zhang, D. Zhang, G. Li, H. Li, *Appl. Catal. B* **2015**, 164, 217-224.
- [20] C. Chen, M. Chen, C. K. Chen, P. C. Wu, P. Chen, M. Basu, S. Hu, D. P. Tsai, R. Liu, *Chem. Commun.* **2015**, 51, 549-552.
- [21] J. Li, Y. Xie, Y. Zhong, Y. Hu, *J. Mater. Chem. A* **2015**, 3, 5474-5481.
- [22] L. Sinatra, A. P. LaGrow, W. Peng, A. R. Kirmani, A. Amassian, H. Idriss, O. M. Bakr, *J. Catal.* **2015**, 322, 109-117.
- [23] S. Zhang, J. Li, X. Wang, Y. Huang, M. Zeng, J. Xu, *J. Mater. Chem. A* **2015**, 3, 10119-10126.
- [24] Y. Ma, X. Wang, Y. Jia, X. Chen, H. Han, C. Li, *Chem. Rev.* **2014**, 114, 9987-10043.
- [25] T. Luttrell, S. Halpegamage, J. Tao, A. Kramer, E. Sutter, M. Batzill, *Sci Rep.* **2014**, 4, 4043-4050.

- [26] H. Tang, K. Prasad, R. Sanjinés, P. E. Schmid, F. Lévy, *J. Appl. Phys.* **1994**, 75, 2042-2047.
- [27] E. Yagi, R. R. Hasiguti, M. Aono, *Phys. Rev. B* **1996**, 54, 7945-7956.
- [28] S. Naya, T. Niwa, T. Kume, H. Tada, *Angew. Chem. Int. Ed.* **2014**, 53, 7305-7309.
- [29] K. Kimuuura, S. Naya, Y. Jin-nouchi, H. Tada, *J. Phys. Chem. C* **2012**, 116, 7111-7117.
- [30] Y. Tang, Z. Jiang, G. Xing, A. Li, P. D. Kanhere, Y. Zhang, T. C. Sum, S. Li, X. Chen, Z. Dong, Z. Chen, *Adv. Funct. Mater.* **2013**, 23, 2932-2940.
- [31] A. Tanaka, K. Hashimoto, H. Kominami, *J. Am. Chem. Soc.* **2013**, 136, 586-589.
- [32] C. Hu, T. Peng, X. Hu, Y. Nie, X. Zhou, J. Qu, H. He, *J. Am. Chem. Soc.* **2010**, 132, 857-862.
- [33] J. Yu, G. Dai, B. Huang, *J. Phys. Chem. C* **2009**, 113, 16394-16401.
- [34] M. Jung, J. N. Hart, D. Boensch, J. Scott, Y. H. Ng, R. Amal, *Appl. Catal. A: Gen.* **2016**, 518, 221-230.
- [35] W. Zhao, M. Zhang, Z. Ai, Y. Yang, H. Xi, Q. Shi, X. Xu, H. Shi, *J. Phys. Chem. C* **2014**, 118, 23117-23125.
- [36] P. Gao, J. Liu, S. Lee, T. Zhang, D. D. Sun, *J. Mater. Chem.* **2012**, 22, 2292-2298.
- [37] J. Zhang, Z. Yu, Z. Gao, H. Ge, S. Zhao, C. Chen, S. Chen, X. Tong, M. Wang, Z. Zheng, Y. Qin, *Angew. Chem. Int. Ed.* **2017**, 56, 816-820.

- [38] B. A. Nail, J. M. Fields, J. Zhao, J. Wang, M. J. Greaney, R. L. Brutchey, F. E. Osterloh, *ACS Nano* **2015**, 9, 5135-5142.
- [39] S. A. Maier, P. G. Kik, H. A. Atwater, *Appl. Phys. Lett.* **2002**, 81, 1714-1716.
- [40] I. Kraljić, C. N. Trumbore, *J. Am. Chem. Soc.* **1965**, 87, 2547-2550.
- [41] H. J. Yun, H. Lee, J. B. Joo, W. Kim, J. Yi, *J. Phys. Chem. C* **2009**, 113, 3050-3055.
- [42] J. Baek, S. Park, C. K. Song, T. Y. Kim, J. Yi, *Chem. Commun.* **2015**, 51, 15019-15022.
- [43] G. Kresse, J. Furthmuller, *Phys. Rev. B* **1996**, 54, 11169-11186.
- [44] J. P. Perdew, K. Burke, M. Ernzerhof, *Phys. Rev. Lett.* **1996**, 77, 3865-3868.
- [45] P. E. Blöchl, *Phys. Rev. B* **1994**, 50, 17953-17979.
- [46] S. L. Dudarev, G. A. Botton, S. Y. Savrasov, C. J. Humphreys, A. P. Sutton, *Phys. Rev. B* **1998**, 57, 1505-1509.
- [47] U. Aschauer, A. Selloni, *Phys. Chem. Chem. Phys.* **2012**, 14, 16595-16602.
- [48] Z. W. She, M. Low, S. Zhang, Z. Liu, A. Mlayah, M. Han, *Adv. Mater.* **2012**, 24, 2310-2314.
- [49] T. Klar, M. Perner, S. Grosse, G. V. Plessen, W. Spirkl, J. Feldmann, *Phys. Rev. Lett.* **1998**, 80, 4249-4252.
- [50] M. Hu, J. Chen, M. Marquez, Y. Xia, G. V. Hartlrad, *J. Phys. Chem. C* **2007**, 111, 12558-12565.
- [51] S. Naya, A. Inoue, H. Tada, *ChemPhysChem* **2011**, 12, 2719-2723.

- [52] A. Houas, H. Lachheb, M. Ksibi, E. Elaloui, C. Guillard, J. Herrmann, *Appl. Catal. B* **2001**, 31, 145-157.
- [53] Y. F. Chen, C. H. Lee, M. Y. Yeng, H. T. Chiu, *J. Cryst. Growth*, **2003**, 247, 363-370.
- [54] S. Watson, D. Beydoun, J. Scott, R. Amal, *J. Nanoparticle Res.* **2004**, 6, 193-207.
- [55] T. Bezrodnaa, G. Puchkovskaa, V. Shymanovskaa, J. Baranb, H. Ratajczak, *J. Mol. Struct.* **2004**, 700, 175-181.
- [56] R. J. Tayade, R. K. Surolia, R. G. Kulkarni, R. V. Jasra, *Sci. Technol. Adv. Mat.* **2007**, 8, 455-462.
- [57] J.-H. Kim, H.-I. Lee, *Korean J. Chem. Eng.* **2004**, 21, 116-122.
- [58] G. Liu, X. Wang, Z. Chen, H.-M. Cheng, G. Q. Lu, *J. Colloid Interface Sci.* **2009**, 329, 331-338.
- [59] H. Wang, T. You, W. Shi, J. Li, L. Guo, *J. Phys. Chem. C* **2012**, 116, 6490-6494.
- [60] S. Yu, Y. H. Kim, H. Y. S. Y. Lee, H. D. Song, J. Yi, *Angew. Chem. Int. Ed.* **2014**, 54, 11203-11207.
- [61] S. Yu, S. Y. Lee, J. Yeo, J. W. Han, J. Yi, *J. Phys. Chem. C* **2014**, 118, 29583-29590.
- [62] M. Ramamoorthy, D. Vanderbilt, R. D. King-Smith, *Phys. Rev. B* **1994**, 49, 16721-16727.
- [63] H. Zhang, J. F. Banfield, *J. Mater Chem.* **1998**, 8, 2073-2076.
- [64] A. Hagfeldt, M. Grätzel, *Chem. Rev.* **1995**, 95, 49-68.
- [65] Z. Zhang, J. T. Yates, *Chem. Rev.* **2012**, 112, 5520-5551.

- [66] D. O. Scanlon, C. W. Dunnill, J. Buckeridge, S. A. Shevlin, A. J. Logsdail, S. M. Woodley, C. R. A. Catlow, M. J. Powell, R. G. Palgrave, I. P. Parkin, G. W. Watson, T. W. Keal, P. Sherwood, A. Walsh, A. A. Sokol, *Nat. Mater.* **2013**, 5, 798-801.
- [67] G. Xiong, R. Shao, T. C. Droubay, A. G. Joly, K. M. Beck, S. A. Chambers, W. P. Hess, *Adv. Funct. Mater.* **2007**, 17, 2133-2138.
- [68] J. Zhao, S. C. Nguyen, R. Ye, B. Ye, H. Weller, G. A. Somorjai, A. P. Alivisatos, F. D. Toste, *ACS Cent. Sci.* **2017**, 3, 482-488.
- [69] J. Sakamoto, T. Ohara, N. Yasumoto, Y. Shiraishi, S. Ichikawa, S. Tanaka, T. Hirai, *J. Am. Chem. Soc.* **2015**, 137, 9324-9332.
- [70] S. Sarina, H. Zhu, Q. Xiao, E. Jaatinen, J. Jia, Y. Huang, Z. Zheng, H. Wu, *Angew. Chem. Int. Ed.* **2014**, 53, 2935-2940.
- [71] G. Hao, B. K. Juluri, Y. B. Zheng, B. Wang, I-K. Chiang, L. Jensen, V. Crespi, P. C. Eklund, T. J. Huang, *J. Phys. Chem. C* **2010**, 114, 18059-18066.
- [72] M. L. Brongersma, N. J. Halas, P. Nordlander, *Nat. Nanotechnol.* **2015**, 10, 25-34.
- [73] C. Clavero, *Nat. Photonics* **2014**, 8, 95-103.
- [74] A. Imanishi, E. Tsuji, Y. Nakato, *J. Phys. Chem. C* **2007**, 111, 2128-2132.
- [75] Y. Shiraishi, H. Sakamoto, Y. Sugano, S. Ichikawa, T. Hirai, *ACS Nano* **2013**, 10, 9287-9297.
- [76] J. Nelson, *The Physics of Solar Cells, Imperial College Press, London* **2003**.

- [77] M. G. Walter, E. L. Warren, J. R. McKone, S. W. Boettcher, Q. Mi, E. A. Santori, N. S. *Chem. Rev.* **2010**, 110, 6446-6473.
- [78] M. X. Tan, C. N. Kenyon, N. S. Lewis, *J. Phys. Chem.* **1994**, 98, 4959-4962.
- [79] M. D. Scanlon, P. Peljo, M. A. Méndez, E. Smirnov, H. H. Girault, *Chem. Sci.* **2015**, 6, 2705-2720.
- [80] D. M. Wood, *Phys. Rev. Lett.* **1981**, 46, 749.
- [81] Z. Ding, H. Yang, J. Liu, W. Dai, X. Chen, X. Wang, X. Fu, *Appl. Catal. B: Environ.* **2011**, 101, 326-332.
- [82] Y. Nosaka, A. Y. Nosaka, *J. Phys. Chem. Lett.* **2016**, 7, 431-434.
- [83] R. Bouwman, W. M. H. Sachtler, *J. Catal.* **1970**, 19, 127-140.
- [84] Z. Zhang, Z. Wang, S.-W. Cao, C. Xue, *J. Phys. Chem. C* **2013**, 117, 25939-25947.
- [85] W.-N. Wang, W.-J. An, B. Ramalingam, S. Mukherjee, D. M. Niedzwiedzki, S. Gangopadhyay, P. Biswas, *J. Am. Chem. Soc.* **2012**, 134, 11276-11281.
- [86] C. Mao, F. Zuo, Y. Hou, X. Bu, P. Feng, *Angew. Chem. Int. Ed.* **2014**, 53, 10485-10489.
- [87] H. J. Yun, D. M. Lee, S. Yu, J. Yoon, H-J. Park, J. Yi, *J. Mol. Catal. A: Chem.* **2013**, 378, 221-226.
- [88] G. Wang, H. Wang, Y. Ling, Y. Tang, X. Yang, R. C. Fitzmorris, C. Wang, J. Z. Zhang, Y. Li, *Nano Lett.* **2011**, 11 3026-3033.
- [89] F. Su, T. Wang, R. Lv, J. Zhang, P. Zhang, J. Lu, J. Gong, *Nanoscale* **2013**, 5, 9001-9009.

- [90] S. Xie, Y. Wang, Q. Zhang, W. Fan, W. Deng, Y. Wang, *Chem. Commun.* **2013**, 49, 2451-2453.
- [91] L. G. Devi, R. kavitha, *Appl. Catal. B: Environ.* **2013**, 140-141, 559-587.
- [92] C. K. Song, J. Baek, T. Y. Kim, S. Yu, J. W. Han, J. Yi, *Appl. Catal. B: Environ.* **2016**, 198, 91-99.
- [93] X. Zhu, C. Jin, X.-S. Li, J.-L. Liu, Z.-G. Sun, C. Shi, X. Li, A.M. Zhu, *ACS Catal.* **2017**, 7, 6514-6524.

## 국문 초록

전세계적으로 발생하는 환경 오염을 해결하기 위해서는 쉽게 얻을 수 있는 에너지원을 기반으로하는 촉매 시스템의 개발이 필수적이다. 광촉매는 촉매의 사용을 위해 추가적인 에너지의 낭비가 필요 없으며 빛이 존재하는 모든 곳에서 사용될 수 있어 많은 주목을 받고 있다. 본 연구에서는 금, 백금 등의 귀금속 나노입자가 가시광선 영역의 빛을 사용할 수 있다는 점에 착안하여, 귀금속이 이산화티탄에 담지된 시스템을 제조하였다. 이산화티탄은 경제적이고 높은 화학적 안정성을 가지고 있으며 독성이 없는 반도체 물질이나, 가시광선 영역의 빛을 거의 흡수할 수 없다는 단점을 가지고 있다. 따라서 가시광선을 이용할 수 있는 귀금속을 접합 시켜 사용할 경우 태양빛을 효율적으로 이용할 수 있는 광촉매 물질이 되므로, 위의 시스템에 집중하여 성능을 향상시킬 수 있는 방법론들을 모색하였다.

첫째로 이산화티탄의 결정상과 형태를 최적화하여 가시광선 영역에서 사용할 수 있는 광촉매의 성능을 향상시키는 연구를 진행하였다. 루타일 결정상으로 이루어진 3차원 형태로 제조되었을 때 금/이산화티탄의 광촉매 시스템들 중 가장 적합함을 확인하였다. 3차원 형태로 이루어진 이산화티탄으로 인해 금에서 국소 표면 플라즈몬 공명의 수명이 증가하고 플라즈몬 상호작용이 발생하였으며, 개선된 광촉매 활성을 확인하였다. 또한, 국소 플라즈몬 공명으로 인해 생성된 열전자들은 아나타아제보다는

루타일 이산화티탄으로 더 효율적으로 전달되었다. 이는 금과 루타일 이산화티탄 전도대 상태 밀도가 겹쳐 전자 전달이 원활하게 일어나는 동시에, 이산화티탄의 큰 밴드 굽힘으로 반대 방향의 전자 전달을 막을 수 있었기 때문이다.

둘째로 금속-반도체 에너지 준위의 조절을 통해 전하상태를 개선하여 높은 성능의 가시광선 감응 광촉매를 개발하고자 하였다. 금속 입자의 크기가 수 나노미터 수준으로 줄어들면 페르미 준위의 뚜렷한 변화를 가져올 수 있으며, 반도체와 접합하였을 경우 반도체의 밴드 굽힘 정도가 달라지게 된다. 모델 시스템으로 백금-루타일 이산화티탄 물질을 사용하였으며, 가시광선 조사 시 협동 전하 분리에 의해 백금 나노입자가 양전하로 하전되었다. 전하 분리의 양과 속도는 이산화티탄 계면에서의 밴드 굽힘 정도를 더욱 증가시킴으로써 더욱 향상되었다. 전하 분리 속도와 실제 광산화 반응의 성능을 비교 관찰하였을 때 두 결과가 깊은 관련이 있음을 확인하여, 금속-반도체 계면에서의 전하 분리가 광촉매 활성화에 가장 중요한 척도임을 판단할 수 있었다.

주요어: 불균일계 촉매, 광촉매, 가시광선, 전하 분리, 에너지 준위, 국부 플라즈몬 공명, 이산화티탄, 금, 백금

학 번: 2014-21589

## List of publications

### International Publications

#### International Academic Published Papers (First Author)

1. H. N. Umh\*, **C. K. Song\***, S. Y. Lee, S. Bae, T. Y. Kim, Y. H. Kim, J. B. Joo, and J. Yi (\*co-first author), “Band alignment modulations of metal-semiconductor system for enhanced charge separation directly related to a photocatalytic performance”, *Catalysis Communications*, **136**, 105921, (2020)
2. **C. K. Song\***, J. Baek\*, T. Y. Kim, S. Yu, J. W. Han, and J. Yi (\*co-first author), Exploring Crystal Phase and Morphology in the TiO<sub>2</sub> Supporting Materials Used for Visible-Light Driven Plasmonic Photocatalyst, *Applied Catalysis B: Environmental*, **341**, 33-43 (2016)

#### International Academic Published Papers (Co-author)

1. Y. S. Yun\*, M. Lee\*, J. Sung, D. Yun, T. Y. Kim, H. Park, K. R. Lee, **C. K. Song**, Y. Kim, J. Lee, Y.-J. Seo, I. K. Song and J. Yi (\*co-first author), “Promoting effect of cerium on MoVTeNb mixed oxide catalyst for oxidative dehydrogenation of ethane to ethylene”, *Applied Catalysis B: Environmental*, **237**, 554-562 (2018)
2. Y. S. Yun\*, H. Park\*, D. Yun, **C. K. Song**, T. Y. Kim, K. R. Lee, Y. Kim, J. W. Han and J. Yi (\*co-first author), “Tuning the electronic state of metal/graphene catalysts for the control of catalytic activity: Via N- and B-doping into graphene”, *Chemical Communications*, **54**, 7147-7150 (2018)

3. T. Y. Kim, **C. K. Song**, Y. S. Yun, D. Yun, J. W. Han, and J. Yi, "Active Site Structure of a Lithium Phosphate Catalyst for the isomerization of 2,3-epoxybutane to 3-buten-2-ol", *Molecular Catalysis*, **445**, 133-141 (2018)
4. J. Baek\*, S. Park\*, **C. K. Song**, T. Y. Kim, I. Nam, J. M. Lee, J. W. Han, and **J. Yi** (\*co-first author), "Radial alignment of c-channel nanorods in 3D porous TiO<sub>2</sub> for eliciting enhanced Li storage performance", *Chemical Communications*, **51**, 15019-15022 (2015)
5. T. Y. Kim\*, J. Baek\*, **C. K. Song**, Y. S. Yun, D. S. Park, W. Kim, J. W. Han, and **J. Yi** (\*co-first author), "Gas-phase Dehydration of Vicinal Diols to Epoxides: Dehydrative Epoxidation over a Cs/SiO<sub>2</sub> Catalyst", *Journal of Catalysis*, **323**, 85-99 (2015)

## Patents

1. 이종협, 백자연, 박수민, **송찬경**, 김태용, 남인호, "삼차원 구조의 구형 타이타니아 제조방법", 대한민국 특허 등록 10-1724395 (2017.04.07)

## International Conferences (First author)

1. **C. K. Song**, H. N Umh, S. Y. Lee, S. Bae, T. Y. Kim, Y. H. Kim, D.-H. Lim, J. B. Joo and J. Yi, "Interpretation of Synergetic Charge Transfer at the Interface of Metal/Semiconductor Photocatalytic System", 2019 North American Catalysis Society Meeting, Hyatt Regency, Chicago, Illinois, USA, 23-June. 28, 2019
2. **C. K. Song**, J. Baek, T. Y. Kim, S. Yu, Y. Kim, J. W. Han, and J. Yi, "Exploring crystal phase and morphology in the TiO<sub>2</sub> for visible-light sensitive plasmonic photocatalyst", 16<sup>th</sup> International Congress on Catalysis, CNCC, Beijing, China, July. 3-July. 8, 2016
3. **C. K. Song**, J. Baek, T. Y. Kim, S. Yu, and J. Yi, "Synthesis of 3D Hierarchical TiO<sub>2</sub> and Its Application to Phenol Photodegradation Reaction",

The Korean Society of Clean Techonology 2014 Fall Meeting, K hotel,  
Gyeongju, Korea, Sep. 24-26, 2014

### International Conferences (Co-author)

1. K. R. Lee, D. Yun, Y. S. Yun, **C. K. Song**, Y. Kim, T. Y. Kim, H. Park and J. Yi, "In Situ Electronic Structure Modulation for Platinum Catalyst in CO Oxidation", 2019 North American Catalysis Society Meeting, Hyatt Regency, Chicago, Illinois, USA, 23-June. 28, 2019
2. Y. Kim, **C. K. Song**, K. R. Lee, T. Y. Kim, H. Park, D. Yun, Y. S. Yun, H. Lee and J. Yi, "Investigation of Structural Change in Li-MoO<sub>3</sub>/SiO<sub>2</sub> Catalyst for Selective Oxidation of Methane", 2019 North American Catalysis Society Meeting, Hyatt Regency, Chicago, Illinois, USA, 23-June. 28, 2019
3. Y. Kim, T. Y. Kim, H. Park, **C. K. Song**, H. Lee, and J. Yi, "The Effect of Oxidants on Methanol Production for Direct Oxidation of Methane over Cu-MOR", The 16th Korea-Japan Symposium on Catalysis, Kaderu 27, Sapporo, Japan, May. 15-May. 17, 2017
4. T. Y. Kim, J. Baek, **C. K. Song**, Y. S. Yun, D. S. Park, W. Kim, and J. Yi, "Production of 1,3-Butadiene from 2,3-Butanediol Using Cesium Oxide Supported Silica Catalyst", 24<sup>th</sup> North American Catalysis Society Meeting, David L. Lawrence Convetion Center, Pittsburgh, Pennsylvania, USA, June. 14-June. 19, 2015
5. T. Y. Kim, J. Baek, **C. K. Song**, J. M. Lee, J. W. Han, and J. Yi, "Heterogeneous Catalytic Process for the Production of 1,3-Butadiene from 2,3-Butanediol", The 15th Korea-Japan Symposium on Catalysis, BEXCO and Haeundae Centum Hotel, Busan, Korea, May. 26-May. 28, 2015
6. S. Park, J. Baek, **C. K. Song**, T. Y. Kim, I. Nam, J. W. Han, and **J. Yi**, "Rational design of 3D TiO<sub>2</sub> for use in Li-ion battery", 227th ECS Meeting, Hilton Chicago, Chicago, Illinois, USA, May. 24-May. 28, 2015

7. T. Kang, **C. K. Song**, Y. Park, and J. Yi, "Preparation of Thiol-Functionalized Mesoporous Silica for the Selective Adsorption of Pt<sup>2+</sup> and Pd<sup>2+</sup>", 10<sup>th</sup> International Conference on Separation Science and Technology (ICSST14), Nara Prefectural New Public Hall, Nara, Japan, Oct. 30-Nov. 1, 2014
8. T. Y. Kim, J. Baek, **C. K. Song**, Y. S. Yun, D. S. Park, and J. Yi, "Density Functional Theory Study on Conversion of Biomass Derived 2,3-Butanediol to 2,3-Epoxybutane", The Korean Society of Clean Technology 2014 Fall Meeting, K hotel, Gyeongju, Korea, Sep. 24-26, 2014

## Domestic Conferences

1. **송찬경**, 엄하늬, 이수영, 배성준, 김용화, 이종협, 주지봉, "협동 전하 분리를 일으킬 수 있는 금속/반도체 광촉매 시스템의 개발과 목표 산화반응에의 응용", 한국화학공학회 2018년도 가을 총회 및 학술대회, 대구 EXCO, 10. 24-26, (2018)
2. 김윤화, **송찬경**, 이경록, 이종협, 이현주, "메탄의 선택적 산화반응에서 Li-MoO<sub>3</sub>/SiO<sub>2</sub> 촉매의 구조 변화 연구", 한국화학공학회 2018년도 가을 총회 및 학술대회, 대구 EXCO, 10. 24-26, (2018)
3. 윤양식, 윤다남, 김태용, 이경록, 박홍석, **송찬경**, 김윤화, 이민재, 성종백, 이종협, 한정우, "구리금속 및 구리-크롬 복합 산화물 촉매에서의 글리세롤 수소화분해 반응 메커니즘 연구", 한국화학공학회 2017년도 봄 총회 및 학술대회, 제주 ICC, 4. 26-28, (2017)
4. 이민재, 윤양식, 성종백, **송찬경**, 이종원, 서영중, 송인규, 이종협, "Ni-Nb-O/Ce<sub>x</sub>Zr<sub>1-x</sub>O<sub>2</sub>의 향상된 산화환원능력을 통한 에탄 산화탈수소반응용 촉매 제조 및 에틸렌 생산능력 평가", 2017년 한국청정기술학회 춘계 학술발표회, 부산 웨스틴조선호텔, 3. 29-31, (2017)
5. **송찬경**, 백자연, 유성주, 김태용, 윤다남, 박홍석, 이경록, **이종협**, "TiO<sub>2</sub> 상과 구조적 효과에 의한 가시광선 영역에서 Au/TiO<sub>2</sub>의 광촉매 활성 분석", 한국화학공학회 2016년도 봄 총회 및 학술대회, 부산 BEXCO, 4. 27-29,

(2016)

6. 백자연, 김태용, 박대성, 박홍석, **송찬경**, 이경록, 이종협, “글루코오스 발효액으로부터의 1,3-부타디엔 생성”, 한국화학공학회 2014년도 봄 총회 및 학술대회, 창원컨벤션센터, 4. 23-25, (2014)
7. 백자연, 김태용, **송찬경**, 이종협, “글루코오스 발효액을 이용한 1,3-부타디엔 생성 반응”, 2014년 한국청정기술학회 춘계 학술발표회, 여수경도리조트, 3. 27-28, (2014)
8. 김태용, 백자연, **송찬경**, 윤양식, 박대성, 한정우, **이종협**, “바이오매스 유래 물질의 맞춤형 탈수반응을 위한 비시널 디올로부터 에폭사이드 유래 물질 생성”, 2014년 한국청정기술학회 춘계 학술발표회, 여수경도리조트, 3. 27-28, (2014)